

Master's Programme in Life Science Technologies

Skull Attenuation Estimation for High-Intensity Focused Ultrasound Using Zero Echo Time MRI

Reetta Kälvälä

© 2025

This work is licensed under a [Creative Commons](https://creativecommons.org/licenses/by-nc-sa/4.0/) “Attribution-NonCommercial-ShareAlike 4.0 International” license.



Author Reetta Kälvälä

Title Skull Attenuation Estimation for High-Intensity Focused Ultrasound Using Zero Echo Time MRI

Degree programme Life Science Technologies

Major Biomedical Engineering

Supervisor Prof. Lauri Parkkonen

Advisor Teija Sainio, PhD

Collaborative partner TYKS

Date 28.8.2025

Number of pages 72+4

Language English

Abstract

Essential and Parkinson’s tremor are among the most common neurological disorders. Magnetic resonance-guided high-intensity focused ultrasound (HIFU) is a minimally invasive surgical procedure that can be used to treat drug-resistant tremor of hands. The high local intensity of focused ultrasound on the brain causes coagulative necrosis, cell death, in the treated intracranial area. In order to estimate ultrasound attenuation and thus, the impact of the skull on treatment outcome, specific skull measurements must be calculated from computed tomography images during the treatment planning.

Zero echo time is a relatively novel magnetic resonance sequence which is suitable for imaging tissues with low water content, which typically exhibit low proton density and consequently, very short T2 relaxation times. This Thesis investigates the feasibility of deriving the required skull attenuation measurements from zero echo time magnetic resonance images. A semi-automatic pipeline is developed to calculate the key skull features using signal intensity detection. Zero echo time images are compared with conventional computed tomography scans via medical image analysis and correlation metrics.

The developed pipeline achieved high and statistically significant correlation between all acquired key measurements. Based on this analysis and the achieved results, zero echo time images show potential as an alternative to computed tomography scans for obtaining skull attenuation measurements for neuro-HIFU treatment planning. Although zero echo time images exhibit slightly lower image quality, contrast, and accuracy in capturing fine structures compared to computed tomography, they can still reproduce the required attenuation estimates with sufficient detail. The findings of this study support the possibility of zero echo time sequence being validated for clinical use.

Keywords magnetic resonance guided high-intensity focused ultrasound, medical image analysis, skull density ratio, zero echo time magnetic resonance imaging, essential and Parkinson’s tremor, HIFU

Tekijä Reetta Kälvälä

Työn nimi Kallon Vaimennusominaisuuksien Arviointi Korkean Intensiteetin
Kohdennettua Ultraääntä Varten Käyttäen Nollakaikuajan MR-kuvausta

Koulutusohjelma Master's Programme in Life Science Technologies

Pääaine Biomedical Engineering

Työn valvoja Prof. Lauri Parkkonen

Työn ohjaaja Teija Sainio, PhD

Yhteistyötaho TYKS

Päivämäärä 28.8.2025

Sivumäärä 72+4

Kieli englanti

Tiivistelmä

Essentiaalinen ja Parkinsonin taudin vapina ovat yleisimpiä neurologisia häiriöitä. Magneettikuvausohjattu korkean intensiteetin kohdennettu ultraääni (HIFU) on minimaalisesti invasiivinen kirurginen toimenpide, jota käytetään käsien lääkeresistentin vapinan hoitoon. Aivojen kohdennetun ultraäänen suuri paikallinen intensiteetti aiheuttaa koagulaatiivisen nekroosin, solukuoleman, hoidetulla alueella. Jotta voidaan arvioida ultraäänen vaimenemistä ja siten kallon vaikutusta hoitotuloksiin, on laskettava tiettyjä kallon vaimennusominaisuuksia kuvaavia arvoja hoitoa suunniteltaessa.

Nollakaikuajan kuvantaminen on suhteellisen uusi magneettiresonanssisekvenssi, joka soveltuu matalan vesipitoisuuden omaavien kudosten kuvantamiseen, joilla on tyypillisesti alhainen protonitiheys ja täten hyvin lyhyet T2-relaksaatioajat. Tässä diplomityössä tutkitaan tarvittavien kallon vaimennusominaisuusarvojen laskemisen mahdollisuutta nollakaikuajan magneettiresonanssikuvista. Nollakaikuajan kuvia verrataan perinteisiin tietokonetomografiakuviin kuva-analyysin ja kehitetyn kallon vaimennusominaisuuksia laskevan puoliautomaattisen algoritmin avulla.

Kehitetty menetelmä saavutti korkean ja tilastollisesti merkittävän korrelaation kaikkien laskettujen arvojen välillä. Analyysin ja tulosten perusteella nollakaikuajan kuvat osoittavat potentiaalia vaihtoehtona tietokonetomografiakuville kallon vaimennusominaisuuksien määrittämiseksi neuro-HIFU -hoidon suunnittelussa. Vaikka nollakaikuajan kuvat osoittavat hieman heikompaa kvanlaatua, kontrastia ja tarkkuutta erityisesti ohuiden rakenteiden tunnistamisessa verrattuna tietokonetomografiakuviin, ne voivat silti toistaa tarvittavat ominaisuudet riittävällä tarkkuudella hoidon suunnittelua varten. Tämän tutkimuksen tulokset tukevat nollakaikuajan magneettiresonanssisekvenssin kliinisen validoinnin mahdollisuutta.

Avainsanat magneettikuvausohjattu korkean intensiteetin kohdennettu ultraääni, kuva-analyysi, kallon tiheysuhde, nollakaikuajan magneettiresonanssikuvaus, essentiaalinen ja Parkinsonin vapina, HIFU

Preface

Although this Thesis was an individual project, it required a great deal of group effort. Special thanks to Teija and Lauri for their valuable guidance throughout the journey, and to the Medical Physics team at TYKS for allowing me to spend this year in their basements working with such a special project. Thanks to Kevin and Itay from Insightec for answering my rather specific questions. Thanks also go to Aalto University for the past incredible six years. And finally, thanks to my friends and Kaarlo for being there all along the way.

Viherlaaksossa, 28.8.2025

Reetta A. Kälvälä

Contents

| | |
|---|-----------|
| Abstract | 3 |
| Abstract (in Finnish) | 4 |
| Preface | 5 |
| Contents | 6 |
| Symbols and abbreviations | 8 |
| 1 Introduction | 10 |
| 1.1 Objectives and research questions | 11 |
| 1.2 Structure of the Thesis | 12 |
| 2 Background | 13 |
| 2.1 Neuro-HIFU in the treatment of tremor | 13 |
| 2.2 Treatment procedure | 14 |
| 2.3 Skull characterization from computed tomography | 14 |
| 2.3.1 Skull density ratio | 15 |
| 2.3.2 Skull feature extraction | 16 |
| 2.4 Zero echo time magnetic resonance imaging | 18 |
| 2.4.1 Sequence | 18 |
| 2.4.2 Skull characteristics calculation | 19 |
| 2.5 Theoretical framework | 20 |
| 3 Research material | 22 |
| 3.1 Patient selection and data | 22 |
| 3.1.1 T1-weighted MR images | 24 |
| 3.1.2 CT images | 25 |
| 3.1.3 ZTE images | 26 |
| 3.1.4 Benchmark SDR | 27 |
| 3.2 Artifacts | 27 |
| 4 Research methods | 28 |
| 4.1 Pipeline | 28 |
| 4.1.1 Helper scripts | 30 |
| 4.2 Preprocessing | 30 |
| 4.2.1 Anonymization | 30 |
| 4.2.2 Format conversion | 31 |
| 4.2.3 Verification | 32 |
| 4.2.4 Preparation | 32 |
| 4.3 Coregistration | 33 |
| 4.3.1 Virtual image domain | 33 |
| 4.3.2 Initialization | 33 |

| | | |
|----------|---|-----------|
| 4.3.3 | Similarity metric | 34 |
| 4.3.4 | Interpolators | 35 |
| 4.3.5 | Optimizer | 35 |
| 4.3.6 | Verification | 35 |
| 4.4 | Image postprocessing | 37 |
| 4.5 | Skull mask creation | 38 |
| 4.5.1 | Platform | 38 |
| 4.5.2 | Region of interest | 38 |
| 4.5.3 | Segmentation protocol | 39 |
| 4.6 | SDR calculation | 41 |
| 4.6.1 | Hemispherical line model | 41 |
| 4.6.2 | Peak detection | 43 |
| 4.6.3 | Algorithm testing | 44 |
| 4.7 | Skull thickness estimation | 45 |
| 4.8 | Statistical analysis | 45 |
| 5 | Results | 47 |
| 5.1 | Registration accuracy | 47 |
| 5.2 | SDR values | 48 |
| 5.3 | Skull thickness | 50 |
| 5.4 | Correlation | 52 |
| 5.4.1 | SDR linear dependencies | 52 |
| 5.4.2 | Accuracy margin | 55 |
| 5.4.3 | Intensity similarity | 56 |
| 5.4.4 | Skull thickness and SDR | 57 |
| 6 | Discussion | 58 |
| 6.1 | Pipeline performance | 58 |
| 6.1.1 | SDR comparability | 59 |
| 6.1.2 | Thickness estimation | 60 |
| 6.1.3 | Visual evaluation | 61 |
| 6.2 | Limitations of the study | 62 |
| 6.3 | Significance and practical implications | 64 |
| 6.4 | Suggestions for further research | 65 |
| 7 | Conclusions | 66 |
| | References | 67 |
| A | Appendix | 73 |
| B | Appendix | 74 |

Symbols and abbreviations

Symbols

| | |
|--------------|---|
| SDR_{CT} | CT-based skull density ratio |
| SDR_{true} | true skull density ratio |
| SDR_{ZTE} | ZTE-based skull density ratio |
| Δt | dead time |
| k_{gap} | gap in the center of the k-space |
| P | number of ultrasound beams from the transducer |
| $\min I_k$ | minimum skull intensity along a ultrasound beam |
| $\max I_k$ | maximum skull intensity along a ultrasound beam |
| r | Pearson correlation coefficient |
| $aTBI$ | average trabecular bone intensity |
| $aCBI$ | average cortical bone intensity |
| N, M | across voxels |
| μ_o | linear attenuation coefficient of tissue |
| μ_{H_2O} | linear attenuation coefficient of water |
| CT_0 | CT number |

Abbreviations

| | |
|------------|---|
| AC–PC line | the anterior commissure–posterior commissure line |
| CT | computed tomography |
| DICOM | Digital Imaging and Communications in Medicine |
| ET | essential tremor |
| FDA | The Food and Drug Administration |
| FID | free induction decay |
| FOV | field of view |
| GUI | graphic user interface |
| HIFU | high-intensity focused ultrasound |
| HU | Hounsfield Unit |
| MAE | mean absolute error |
| MMI | Matte’s Mutual Information |
| MR | magnetic resonance |
| MRgFUS | MR guided high-intensity focused ultrasound |
| NifTI | neuroimaging informatics technology initiative |
| LAS | left, anterior, superior |
| LPS | left, posterior, superior |
| PD | Parkinson’s disease |
| RAS | right, anterior, superior |
| RF | radiofrequency |
| RMSE | root mean squared error |
| ROI | region of interest |
| SDR | skull density ratio |
| SimpleITK | Simple Insight Toolkit |
| SNR | signal-to-noise ratio |
| SD | standard deviation |
| SS | skull score |
| TR | repetition time |
| TYKS | Turku University Hospital |
| VIM | ventral intermediate nucleus of the thalamus |
| ZTE | zero echo time |

1 Introduction

Magnetic resonance (MR) guided high-intensity focused ultrasound (HIFU, MRgFUS) is a minimally invasive surgical procedure used to treat drug-resistant essential and Parkinson's tremor of the hands [1, 2]. Focused ultrasound has previously been used to treat uterus and prostate tumors, but Turku University Hospital (TYKS) was the first Nordic hospital to start neuro-HIFU thalamotomies in 2022 [1]. The HIFU procedure utilizes over 1000 piezoelectric transducers distributed on a spherical surface to achieve precise acoustic focusing of an ultrasound beam exceeding 20 kHz onto a localized intracranial target [1]. Due to the high ultrasound intensity ($100\text{--}10\,000 \frac{W}{cm^3}$) in the focal point, as small as $1.5 \times 1.5 \times 3 \text{ mm}^3$, the temperature is elevated above $55 \text{ }^\circ\text{C}$ leading the soft tissue to coagulative necrosis and cell death [3, 1].

In tremor treatment with HIFU, the intensity and temperature achieved in the focal point depend on the density and thickness of the skull of the patient, the precision of phase correction of the machine, and on physiological properties, such as blood flow in the tissue [4, 1]. Generally, the high acoustic impedance of the skull has an impact on the HIFU procedure in two ways: the focus of the ultrasound beams can be affected due to reflections, refractions, and aberrations, and secondly, by overheating the head due to ultrasound absorption in bone tissue [5]. As the ultrasound beam progresses through different layers of tissue on its way to the target, its speed changes. Due to the variation of relative time shifts in the wavefront, the amplitude decreases and the waveform is distorted, and therefore the focal point is widened and shifted spatially [6]. To predict the impact of the skull on the progression and attenuation of the beam on the tissue, a skull density ratio (SDR) is calculated for each patient while planning the treatment [1]. The lower the SDR, the more the skull resists ultrasound beams and the less likely it is that a therapeutic temperature will be reached at the focus [1]. As SDR is one of the measures that determines the patient's suitability for the treatment, a higher SDR is desired, as it suggests a better treatment result.

The skull density ratio is often calculated as the ratio between the density of the trabecular bone and the density of the cortical bone, or as the mean ratio of the minimum and maximum skull intensities along each ultrasound beam [7, 8]. The Food and Drug Administration (FDA) has limited the use of HIFU to patients with SDR greater than 0.45 ± 0.05 , calculated by the HIFU system [7]. To accept a patient for HIFU treatment in TYKS, the patient's SDR must be at least 0.35 [1]. Due to different skull characteristics, not all tremor patients are suitable for neuro-HIFU treatment because their low skull density ratio prevents achieving the therapeutic temperature [8, 1]. Currently in TYKS, a computed tomography (CT) scan is obtained from each patient before the treatment to determine whether their SDR is suitable for the treatment [1]. In addition, the CT scan is used by the HIFU system to correct the phase difference caused by the boundaries of the skull tissue during the treatment [1].

CT scans have traditionally been the preferred imaging modality for dense bone structures such as the skull. However, zero echo time (ZTE) is a relatively novel MRI sequence that is suitable for imaging tissues with low water content, which typically exhibit low proton density and very short T2 relaxation times [9]. As cortical bone

has a T2 relaxation time close to $390 \mu\text{s}$ with 3T, ZTE is sufficient in producing good contrast images from cranial bones similar to those obtained with CT [10]. Although the clinical usability of ZTE images has been studied, not many studies compare the ZTE-based SDR to the true SDR of a patient. Some studies suggest that calculating the SDR from ZTE images might be possible with certain accuracy, although the Pearson correlation coefficients and corresponding p -values are not widely available. However, for example, Caballero and colleagues have found a significant correlation in SDRs calculated from CT and ZTE images [5].

Although preliminary results have been promising with smaller datasets, MRI-based SDR calculation has not yet been validated for clinical use. The few existing studies rely on threshold-based bone tissue segmentation for calculating the ratio of trabecular to cortical bone density. This approach introduces significant uncertainty due to the partial volume effect especially present on tissue boundaries and near fine structures. In addition, to our current knowledge, SDR values have not been calculated from ZTE images acquired with a state-of-the-art GE SIGNA Premier 3T scanner. To overcome threshold-derived uncertainties, this Thesis uses an intensity-profile-based SDR approach, which was not present in previous studies. The goal is to investigate the possibility of using ZTE MRI instead of CT scans to determine a patient's SDR prior to HIFU treatment.

1.1 Objectives and research questions

The primary objective of this Master's Thesis is to investigate the suitability of using ZTE MRI as a clinically usable alternative for CT imaging in the context of HIFU treatment planning. ZTE offers several practical advantages, including the resistance to artifacts without the use of ionizing radiation. This may support its potential as a substitute for CT, particularly in imaging dense but fine bone structures, such as the skull.

This Thesis aims to assess the capability of ZTE MRI to accurately determine a patient's SDR prior to HIFU treatment, thereby reducing radiation exposure, shortening preparation time, and simplifying clinical workflows. This is done by developing an intensity-based semi-automatic analysis pipeline that utilizes a total of $n = 35$ neuro-HIFU patients' ZTE images, T1-weighted MR images, and their CT scans. The pipeline first coregisters the CT and ZTE images to the same anatomical space, after which the skull calvaria caps are segmented, and the skull thickness and intensity-based measurements are calculated. The statistical correlation between the derived measurements is assessed and examined. In addition, the pipeline is used to calculate the same measures from $m = 6$ patients' unconventional CT images, in order to obtain information from previously used modality.

Based on these objectives, the Thesis aims to answer the following research questions:

1. Can GE SIGNA Premier 3T ZTE MRI provide sufficient anatomical detail for HIFU treatment planning?
2. How do the image quality and clinical utility of ZTE compare to conventional CT in the context of HIFU planning?
3. Can SDR and other skull measurements be calculated in statistically significant detail from the ZTE images, and do they correlate with the conventionally acquired measurements?

This Thesis was conducted at the request of TYKS, with the analysis performed under the supervision of the Medical Physics Department. The results are directly usable for neuro-HIFU research and in the planning of further clinical validation. This study applies the Data Protection Regulation and the Act on the Secondary Use of Social and Health Information (Laki sosiaali- ja terveystietojen toissijaisesta käytöstä 2019/552). The service provider has the right to process and combine identifiable customer data in its registers if it is necessary for the development, monitoring, and planning of operations. The processing of data is carried out in accordance with the objectives of the research, respecting data protection and privacy.

1.2 Structure of the Thesis

This Thesis is organized into seven chapters, beginning with an introduction and overview of the background and ending with conclusions and future directions. Chapter 2 provides background information and a literature review on neuro-HIFU thalamotomy, with focus on patient preparation, skull density ratio calculation, and computed tomography, which is currently used in clinical practice. In addition, the suggested alternative, zero echo time magnetic resonance imaging sequence, is introduced. Finally, the theoretical framework of this study is outlined.

The following chapters present the quantitative research and its approaches. Chapter 3 outlines the research material and patient selection criteria. Chapter 4 describes the research methods in detail, including data anonymization procedures, and additional scripts used in the study, as well as data preprocessing, image coregistration, bone segmentation, and the intensity-based algorithm designed for the SDR and skull thickness computation. The Chapter also outlines the correlation analysis used to compare CT- and ZTE-based SDRs.

The results of the study are introduced in Chapter 5, which presents the outcome of the SDR comparison and statistical analysis, while Chapter 6 offers a critical discussion of the findings in relation to the clinical context and existing literature. In addition, the research contributions, practical implications, limitations, and suggestions for future research are presented. Finally, Chapter 7 concludes the Thesis by summarizing the main findings and their implications.

References are listed following the main text, and the Appendices A–B at the end of the Thesis include additional materials and technical details relevant to the study.

2 Background

This Chapter summarizes the relevant literature, introduces the foundation of the modalities related to the study, as well as outlines the theoretical framework of this Thesis. The neuro-HIFU treatment procedure is introduced in Chapters 2.1–2.2. The skull structure of an adult Caucasian is introduced in Section 2.3, together with the skull density ratio calculation, and the basis of computed tomography. The proposed ZTE sequence and its usability in skull feature extraction is presented in Section 2.4. Lastly, the theoretical framework is outlined in Section 2.5, before the study-related Chapters begin.

2.1 Neuro-HIFU in the treatment of tremor

Essential (ET) and Parkinson's (PD) tremor are among the most prevalent neurological disorders globally, both affecting the patient's daily life significantly [11, 12]. The most recurrent symptom in patients with ET is the kinetic tremor of arms during voluntary movements. The tremor eventually progresses into inability to perform daily tasks [11]. Patients with severe ET also have a postural tremor, and they may also have non-motor difficulties, such as cognitive impairment and neuropsychiatric symptoms [11, 13]. Parkinson's disease is a neurodegenerative disorder, where dopaminergic neurons experience early prominent death [12]. Patients with PD have clinically relevant heterogeneous motor and non-motor issues, including bradykinesia, rest tremor, olfactory dysfunction and cognitive impairment [12]. The cause of both, ET and PD, is believed to lie in genetics, together with environmental and habit-related factors [13, 12, 14]. Treatment options for patients with medically intractable ET and tremor-dominant PD include deep brain stimulation and high-intensity focused ultrasound thalamotomy [13, 2].

High-intensity focused ultrasound thalamotomy is a minimally invasive procedure that is used to treat tremor patients by delivering focused acoustic energy to discrete intracerebral targets. The focused ultrasound induces localized thermal ablation via coagulative necrosis and cellular apoptosis while preserving the surrounding brain tissue [2, 1]. The selected area for treatment of PD and ET tremor is the ventral intermediate nucleus of the thalamus (VIM), which is the tremor source for the contralateral hand [2, 1]. The VIM is located next to the pathway connecting cerebellum, red nucleus, and thalamus, and it cannot be visualized with standard clinical MRI sequences [15, 1]. The VIM is sufficient target for HIFU because it is part of the cerebello–thalamo–cortical tremor network and thus, the lesion suppresses the transfer of tremor signals between the cerebellum and the motor cortex [16, 17].

Before the treatment, MR and CT images are acquired to assess the patient's suitability for HIFU, and to conclude a treatment plan [1, 18]. The procedure preparation may also include tractography imaging to validate the location of the target, and to avoid vital pathways near it [1]. As the VIM cannot be visualized with standard MRI sequences, anatomical landmarks, such as the anterior commissure–posterior commissure line (AC–PC line), are used to estimate the location [17].

2.2 Treatment procedure

The patient preparation steps include shaving the patients head to decrease the amount of air that could cause coagulation, possible medication, and installation of the stereotactic frame to prevent the impact of tremor to the treatment[1, 19]. A water-filled membrane is attached over the stereotactic frame to serve as a coupling medium to dissipate the excess heat generated by the focused ultrasound; the frame is attached to the MRI table to ensure precise targeting and immobilization The target is identified and marked during the last preparation scans[1, 19]. The HIFU treatment is performed in MRI guidance to allow the temperature and heat dose to be monitored in the target area, as well as to focus the ultrasound beams as intended during the procedure [1, 18, 19].

The VIM sonications are done in multiple steps to monitor the patient's response to the treatment. The preliminary low-dose sonications are performed by raising the temperature of the target area to approximately 45 degrees, after which the necessary corrections are made in all three slice orientations [1]. A verification lesion is done by raising the temperature up to 50 degrees in order to create a temporary response and to see the possible adverse effects [1]. If the patient's physical response is sufficient, the permanent lesion process may begin [1]. The permanent VIM lesions are made by increasing the focal temperature within 55–60 degrees for a few seconds [20]. As the sonications are done in multiple sets, they are separated with off-times to allow the adjacent tissue to cool down [20, 18]. The accumulated thermal dose accounts for spatial-shifting artifacts to merge thermal data accurately during the procedure [20, 18]. The neurologist continuously monitors the patient and the change and reduction of tremor during the treatment [18]. In addition, the temperature elevation, accumulated thermal dose, spatial maps of induced coagulation, cavitation, and the created lesion are monitored closely during the procedure [18].

As the treated region cannot be directly visualized during the treatment, the results are assessed immediately after the procedure with T2-weighted MR images, where the created lesion can be visualized [1]. After successful ablation, the tremor of the targeted contralateral hand is reduced instantly.

2.3 Skull characterization from computed tomography

The human skull comprises 22 distinct bones, each with unique morphological characteristics [21]. The structure of the skull is composed of two types of bone arranged in three layers. The outer layers, known as the cortical tables, consists of dense cortical bone, while the inner layer contains spongy trabecular bone [22].

In the treatment of PD and ET hand tremor using HIFU, the ultrasound intensity and temperature achieved at the focal point are influenced by several factors. These include the ultrasound energy attenuation by the patient's skull tissue, dependent on its density and thickness, the accuracy of the machine's phase correction, and physiological properties such as blood flow in tissue [1]. As the acoustic, mechanical, ultrasound waves from the HIFU transducer pass through the different medium interfaces, they experience attenuation and thus, energy loss. The most common loss mechanisms

are reflection, scattering, and mode conversion [23]. Once the ultrasound wave propagates from connective tissue to bone, it experiences reflection. In addition, a mode conversion occurs between longitudinal and shear waves, and thus the mechanical ultrasound wave is scattered due to the microstructure of the skull [23]. The energy absorbed by the skull converts into heat, changing the speed of the wave [23]. Due to the variation in relative time shifts in the wavefront, the amplitude decreases and the waveform is distorted, and therefore, the target focal point in VIM may be widened and shifted spatially [6].

Therefore, accurately estimating the ultrasound propagation through the skull is vital for effective HIFU thalamotomy. However, the skull's complex internal structure and geographical variability make this prediction challenging. The anatomy of the skull changes over a person's lifetime. In addition to that, each skull is not only anatomically and structurally unique, but its properties also vary in different regions and developmental stages. This inherent variability makes it challenging to estimate the acoustics of the skull using only a single measure.

2.3.1 Skull density ratio

The skull density ratio (SDR) models the efficiency and prediction accuracy with which ultrasound energy can penetrate the skull. It has been studied that out of all possible skull measurements, the SDR is the most prominent stand-alone variable in predicting the efficiency of a HIFU treatment and the attenuation properties of the skull [24]. The skull thickness itself does not correlate with the treatment outcome, but with the skull volume, which has proven to affect with the outcome [24].

Therefore, the SDR is used to determine the patient's suitability for HIFU treatment: the lower the SDR, the more the skull resists the ultrasound beam and the less likely it is that the therapeutic temperature will be reached in the focus [1]. The SDR can be calculated via two different methods: as the mean Hounsfield units (HU) ratio of the density of the trabecular bone and the density of the cortical bone, or as the mean ratio of the the minimum and the maximum skull intensity values along each ultrasound beam [7, 25, 8]. Both methods rely on the same mathematical principles, and thus the calculated skull density ratio varies from 0 to 1. The FDA has limited the use of neuro-HIFU (Insightec Ltd., Tirat Carmel, Israel) in the United States to patients with SDR greater than 0.45 ± 0.05 [7, 26]. Based on numerous publications, the empirically decided SDR of 0.3–0.35 is generally recommended for thalamic targets for Caucasian patients in Europe [27, 28, 29, 8].

If the structure of the skull is very uniform, the difference in the skull tissue interfaces is acoustically favorable, and thus the ultrasound beam does not experience as many loss mechanisms as in the interface of tissues with larger density differences. Therefore, a higher SDR is generally associated with a preferable treatment outcome due to the skull being more homogeneous. In a recent study, Ng and colleagues studied the impact of the SDR on the treatment outcome of $n = 270$ patients, from which 31 had a low SDR and 239 had a high SDR [25]. Ng and colleagues determined with case-matched and non-case-matched analyses that patients in the low SDR group required significantly higher maximum sonication power, duration, and energy, and

reached lower maximum temperatures with smaller lesions, compared to patients with a higher SDR [25]. The study also concluded that the low SDR cohort had a higher chance of a procedure failure due to the lesion not reaching the desired size [25]. Thus, for a patient to be accepted for safe HIFU treatment at TYKS, the patient's SDR must be at least 0.35, although treating patients with even lower SDR may be technically possible [1, 7].

2.3.2 Skull feature extraction

As studies suggest that a patient's age, sex, and skull thickness are uncorrelated with their SDR, deriving the patient's SDR is not possible based on the external measures [30, 24]. Thus, computed tomography scans are used to determine the skull density ratio of a patient prior to the treatment. Computed tomography utilizes a synchronously rotating X-ray tube, together with multiple detectors to record a series of one-dimensional projections from the object [31]. The computed tomography image is reconstructed to be a map of the tissue CT numbers, instead of being a display map of spatially-dependent tissue attenuation coefficients [31]. The CT_0 numbers in Hounsfield units are calculated via

$$CT_0 = 1000 \frac{\mu_0 - \mu_{H_2O}}{\mu_{H_2O}}, \quad (1)$$

where μ_0 is the linear attenuation coefficient of the tissue and μ_{H_2O} is the linear attenuation coefficient of water in each pixel of the image [31]. The attenuation coefficients are dependent on the photon energy of the beam.

It has been widely accredited that the HU value is a quantitative measurement of the density of the bone, and it has been recognized as the principal method for bone quality and density examination [32, 33]. The CT number values generally have a range from -1000 to $+3000$, and the highest number corresponds to dense bone, whereas air produces the lowest number [31]. Due to its high X-ray attenuation properties, bone is displayed in white color in CT scans and air as black.

The two common methods for calculating the skull density ratio from CT images are the skull score (SS) and the skull density ratio. According to Tsai and colleagues, and the interview of Tsai and Rachmilevitch from Insightec, the automatic skull score of the CT images uploaded to their ExAblate Neuro 4000 HIFU platform is calculated via

$$SS = \frac{\sum_{k=1}^P \min(I_k) / \max(I_k)}{P}, \quad (2)$$

where P indicates the number of ultrasound beams from the transducer, $\min(I_k)$ is the minimum and $\max(I_k)$ is the maximum skull intensity along each beam accordingly [8].

Thus, the SS is the mean across all minimum and maximum skull intensity ratios through the skull, along all ultrasound beam paths from the transducer to the target [8]. Therefore, per Equation 2, high SS in CT images is achieved by a low intensity difference between the cortical and trabecular bone. This would mean that the skull of high SS patient is more uniform and thus, it causes less reflections, refractions,

aberrations, and overall energy attenuation, together with less heating in the skull. Therefore, allowing higher energy transfer from the ultrasound beam to the target tissue.

This finding was supported by the group of Tsai when they confirmed that the contrast between the cortical and the trabecular bone was higher in the low SS CT images and lower in the high SS images [8]. However, it should be noted that Tsai and colleagues contradictorily mention in their results section that "According to the Equation, a high intensity difference between the cortical and trabecular bone would lead to a high SS.", which Tsai four years later confirmed to be an error in the paper [8, 34]. A similar SS Equation has been used by the group of Chupova three years later in their acoustic modeling study. They simulated the aberrations caused by an ultrasound beam passing through the skull [35]. Chupova and colleagues calculated the SS similarly to Tsai and colleagues, also by drawing the ultrasound beams from each HIFU element to the focal point, and by taking the mean ratio of the minimum and maximum Hounsfield unit values along the beam [35]. Thus, the SS of the patient is the average of all obtained ratios in both studies [35, 8].

According to the interview and the email conversation with Tsai and Rachmilevitch, the Insightec software model only takes into account the outer cortical layer and the trabecular bone tissue in the path of each beam. Thus, leaving the inner cortical layer of the skull outside of their model, also in use in TYKS. [34, 36].

Although the SS is used in some studies and utilized by the Insightec software, generally, the SDR is used more widely in neuro-HIFU-related studies. This is because the full SS estimation algorithm is unknown to the public. The general SDR calculation is done by first segmenting the cortical bone and trabecular bone of the skull, and then dividing the averaged trabecular bone CT image intensity by the average cortical CT image intensity [8]. According to Tsai and colleagues, the general SDR is derived as

$$aTBI = \frac{\sum_{i=1}^N TBI_i}{N}, \quad aCBI = \frac{\sum_{j=1}^M CBI_j}{M}, \quad SDR = \frac{aTBI}{aCBI}, \quad (3)$$

where $aTBI$ is the average trabecular bone intensity divided by the average cortical bone intensity ($aCBI$) across all voxels N and M [8, 34].

Thus, the SDR provides a direct method for estimating skull attenuation properties, while the SS accounts for the acoustic properties of the skull. The SDR Equation (3) is more widely established in the field than the more precise skull score Equation (2).

However, the segmentation of the trabecular and cortical bone required in the SDR calculation has major limitations due to the partial volume effect, which appears when the thickness of the tissue is less than the voxel size of the image. According to an extensive study performed by the group of Adanty, the thickness of the human trabecular bone tissue in the skull can be under 0.1 mm, which is less than the voxel size of most clinical CT machines [37]. Thus, making the general SDR an unreliable method for calculating the attenuation properties of the skull. On the other hand, the value obtained via the SS-method may vary depending on the image preprocessing performed, as the change in the image contrast will have an impact on the maximum and minimum intensities in the image. In addition, it can be seen from Equation 2

that a small P , meaning a small amount of line intensity paths through the skull, will result in an unreliable and non-generalizable result for the SS. Therefore, the number of intensity line paths must be chosen accordingly.

However, it has been confirmed that the SS and SDR values of a patient's skull are highly correlated. Per Tsai and colleagues, the Pearson correlation of the SS and SDR of $n = 246$ patients was $r = 0.81$ with p -value under 10^{-5} [8]. However, according to the study later done by Chupova and colleagues, the SDR and SS they calculated for their ($n = 1$) patient were the same, even though Tsai and colleagues concluded earlier in their study that the SS should generally be higher than the SDR of the patient [35, 8]. This is due to the fact that the SS is more sensitive than the SDR to the difference between the cortical and trabecular bone tissue [8]. Tsai and colleagues concluded that an SS of one should produce an SDR of 0.85 per the linear relationship of the two measures [8].

Both skull attenuation estimation methods, the SS and the SDR, have their caveats; SS being more prone to the influence of image preprocessing, and SDR being systematically incorrectly estimated due to the partial volume effect present in all clinical CT images. Due to the aforementioned reasons regarding the SDRs inaccuracy, this study will utilize the SS to estimate the attenuation properties of the skull, although the complete SS calculation algorithm and the image preprocessing methods used by the HIFU system are not available to the public. Going forward, due to the HIFU nomenclature the term skull density ratio, SDR, refers to the SS value calculated via Equation 2 in this Thesis.

2.4 Zero echo time magnetic resonance imaging

Zero echo time is a relatively novel MRI sequence capable of imaging dense, low water content structures, such as the cortical bone. It is optimal for tissues with low proton density and consequently, very short T2 relaxation times [9]. The zero echo time sequence utilizes ultrafast readout to detect the free induction decay (FID) signal, thus differing from other conventional MRI sequences that detect the signal echoes [38]. As the cortical bone has a T2 relaxation time close to $390 \mu\text{s}$ with 3T, ZTE is sufficient in producing good contrast cranial bone images, similar to those obtained by CT [10]. The advantages of the ZTE sequence include silent scanning, robustness against artifacts, and being a MR sequence, it does not rely on ionizing radiation [38]. Previous research has confirmed that ZTE images can be clinically viable and that it can replicate the clinical information present in conventional CT scans [10, 9, 39, 40].

2.4.1 Sequence

Zero echo time imaging achieves a near-zero time interval between the radiofrequency (RF) excitation pulse and the signal acquisition [39]. The base of the sequence lies in non-selective volume excitation, 3D-radial center-out k-space encoding, and a small flip angle [38]. Unlike other RF pulse sequences, ZTE starts the readout of the FID signal immediately after the RF pulse [40]. Thus, it requires high-performance coils equipped with rapid transmit/receive switching capabilities [39]. During the RF pulse,

the readout gradient is on to achieve a zero echo time and to have maximum k-space speed [41]. The imaging procedure is optimized in a similar manner as conventional MRI sequences: via adjustments of bandwidth, the field of view (FOV), flip angle, and image matrix [40]. A simplified schematic of the general ZTE sequence is presented in Figure 1.

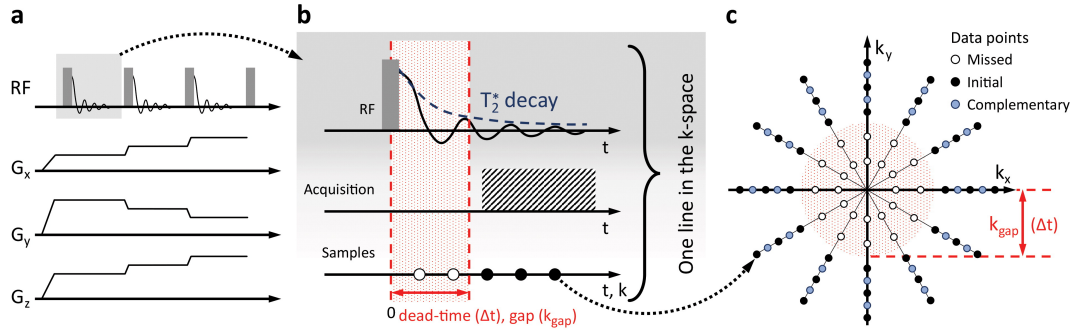


Figure 1: Simplified illustration of a typical ZTE sequence capturing the free induction decay of the tissue (not in scale). (a) Before the initial RF pulse, the gradients are ramped up and they remain on during the entire sequence. (b) A dead time (Δt) occurs after the RF pulse and the signal cannot be acquired during it. Therefore, a non-filled spherical gap occurs (c) in the center of the k-space (k_{gap}). After each RF pulse, a new radial spoke is obtained to eventually fill the entire k-space volume. Oversampling and other strategies are used to fill the center gap and to improve the signal-to-noise ratio (SNR) across the image. Figure from Aydingoz and colleagues from Reference 40.

2.4.2 Skull characteristics calculation

Given its unique imaging properties and good contrast in bone, the ZTE MRI sequence represents a promising alternative to CT in neuro-HIFU treatment planning. As HIFU patients undergo MR imaging as part of the treatment planning procedure, excluding the CT imaging would not only make the planning phase cheaper, faster and more convenient, but also reduce the radiation dose of the patients.

Although deriving skull measures from ZTE images has been studied, none of them compare the ZTE-based SDR to the true SDR of a patient using an intensity-based approach. Some studies suggest that calculating the SDR from ZTE images might be possible with certain accuracy. Therefore, this Thesis aims to investigate the feasibility of ZTE images in SDR calculation.

One of the only available studies assessing the relationship of ZTE- and CT-derived SDRs is performed by Caballero and colleagues [5]. They found a significant correlation ($r^2 = 0.80$, $p < 0.05$) in SDRs calculated from CT and ZTE-based measures using threshold segmentation and morphological methods in 2019 [5]. The study was performed with $n = 16$ (7 women, 9 men) tremor patients, whose SDRs were greater than 0.3. Caballero and colleagues coregistered the patients' CT and ZTE images to their native spaces and segmented the skull tissues to calculate eight different measures, including the skull thickness, the SDR, and the angle of incidence [5]. They

concluded that the skull properties extracted from the CT images were extremely close to those extracted from the ZTE images [5].

However, they concluded that some local measures were not similarly replicated in ZTE images compared to CT images [5]. In addition, they found that the SDR is more correlated with skull thickness when measured with ZTE, which might be due to the low spatial resolution of 1 mm^3 , acquisition matrix of 256 by 256, and FOV of 256 by 256 mm^2 in the ZTE images, or due to the low number of participants in the study [5]. Therefore, it must be noted that the SDR is likely to be overestimated in the case of thinner skulls due to the partial volume effect. Based on a broad microCT skull bone segmentation study by Lillie and colleagues, the trabecular bone thickness in the skull may be on the sub millimeter scale in the parietal bone [21]. Although Caballero and colleagues found a significant correlation between the two modalities, it is likely that the results include a great source of error due to the partial volume effects and low resolution of the ZTE and CT images [5]. Thus, making the direct thresholding and morphological approach and thus, the usage of Equation 3 unsuitable approach for an analysis of this kind [5].

In another study, Cho and colleagues compared the CT and ZTE images of head trauma patients ($n = 13$) in a clinical setting [9]. The aim of their study was to assess the diagnostic image quality of the ZTE images. The authors were able to reliably diagnose all fractures present in the CT images from the ZTE images [9]. The skull thicknesses measured from the CT and the ZTE images were close to the same ($r^2 = 0.997$, $p = 0.09$) [9]. They concluded that the ZTE images have diagnostic image quality comparable to CT images, although the spatial resolution of ZTE is often lower than that of a high-quality CT image [9]. The obtained p -values were relatively high, most likely due to the low sample size.

Studies show that the limited spatial resolution of $0.8\text{--}1 \text{ mm}^2$ of ZTE images compared to the resolution of $0.5\text{--}0.6 \text{ mm}^2$ of CT images poses a significant practical limitation for the method [5, 38]. The difference in spatial resolution is due to the limitations in hardware of currently available MRI platforms [38]. Another challenge in neuroimaging applications for the ZTE is the naturally low SNR of weak bone signal, together with the complex anatomy and pathology of the head and neck [10]. The complex pathology can result in false positives with e.g., fibrous tissue and cartilage, which also have a short T2 time, as well as false negatives in, e.g., thin, unmineralized, and irregular bones [38]. Although zero echo time imaging has not been widely implemented in clinical use yet, it does have some clinically validated applications, such as in the evaluation of osteoarthritis and shoulder dislocations [42]. In addition, it has potential in other musculoskeletal applications, such as in developmental and traumatic radiology [40]. It is expected that the evolving MRI hardware and software markets will likely find a solution to overcome these restrictions in the near future.

2.5 Theoretical framework

Building on the imaging principles discussed in the previous sections, this Thesis outlines the basis for the possibility of replacing CT with ZTE in SDR estimation for neuro-HIFU treatment planning. Although there exist over a hundred HIFU-

related skull density ratio publications in Google Scholar, roughly a few tens of them concentrate on the calculation of the SDR, only a few include a ZTE-based estimation, and none of them has studied ZTE images acquired with the top-grade GE SIGNA Premier 3T scanner.

Most of the aforementioned studies have been performed with small datasets of 1–20 patients using a threshold-based segmentation protocol for the cortical and trabecular bone, which is likely to produce insufficient results due to the partial volume effects and resolution issues, as confirmed by Herbst and colleagues [33]. Per Herbst and colleagues, segmenting the trabecular and cortical bone is not accurately possible from normal CT scans, which most SDR studies utilize [33].

The underlying assumption in this Thesis is that ZTE MRI, due to its ability to capture signals from low proton density tissues such as the skull, can produce imaging data comparable to CT. This Thesis expects that the ZTE intensities are comparable to the HU values of CT image, when it comes to the skull density and consequently, bone tissue attenuation estimation. Therefore, it can be rationalized that the skull density calculation would be possible from sufficient ZTE images, as it is possible for CT images. Thus, by coregistering the CT and ZTE images to the anatomical MR image space using an affine transformation and performing skull volume segmentation, it is theoretically possible to calculate the SDR with Equation 2.

Segmentation of the skull volume from ZTE images relies on intensity-based thresholding techniques, which are commonly used to CT images as well. The acquired skull volumes can be used to generate a sufficient number of intensity profiles through them and to calculate SDR values from the profiles. The resulting SDR_{ZTE} values can then be statistically compared to the SDR_{CT} measures, and the ground truth SDR_{true} measures calculated by the Insightec HIFU system to assess the clinical validity of the calculation algorithm and eventually, the performance of the ZTE images in SDR calculation.

The quality and spatial resolution of the images used in this analysis are higher than in most studies introduced in this Thesis. Therefore, this Thesis assumes that by applying a reasonable amount of image preprocessing, such as bias field correction for the ZTE images and high-pass filtering for both modalities, the results would be robust and reliable. It is also supposed that the intensity line paths, placed radially through the skull volume, do not need to represent the actual path of the ultrasound beams that distort due to refraction, if the used number of paths is high enough.

The analysis pipeline created for this Thesis assumes that the primary source of variability lies in signal intensity rather than in the morphological aspects, and that the ZTE signal strength within bone is a valid surrogate for CT images.

3 Research material

This Chapter presents the research material used in the study. Section 3.1 will offer an overview of the patient selection and data collection protocol. Sections 3.1.1–3.1.4 will describe the three types of imaging data: anatomical T1-weighted MRI, ZTE and CT, and the benchmark SDR data used in the study. Lastly, Section 3.2 will assess the main artifacts affecting the images used.

The data used in this study include all patients who have undergone HIFU treatment at TYKS between July 2022 and June 2025, and whose data met the requirements. The study included total of $n = 35$ patients, 19 men and 16 women, all with age over 65. The dataset is divided into two subsets based on the CT scanner used to acquire the pretreatment CT images. The main subset consists of $n = 29$ patients' conventional CT, ZTE and anatomical MR images, all acquired after December 2023. The other subset includes $m = 6$ patient's unconventional CT scans and their corresponding ZTE, and T1-weighted MR images, acquired before December of 2023. This subset of $m = 6$ older images are included in the analysis not to acquire statistically significant information, but in order to get an overall picture of the previously used CT modality.

3.1 Patient selection and data

The patient selection protocol ensures that all data are compatible, without major artifacts. The patients included in this study were selected if they met all of the following requirements:

1. The patient has an SDR greater than 0.35, determined by the Insightec HIFU system.
2. Patient's all images (T1 MRI, CT, ZTE) have been acquired at TYKS with the following machines during the given timeline:
 - (a) T1 MR images with GE SIGNA Premier 3T scanner.
 - (b) CT images with GE Medical Systems Revolution Apex CT scanner, after December 2023 or with Toshiba Aquilion ONE CT scanner before December 2023.
 - (c) ZTE MR images with GE SIGNA Premier 3T scanner.
3. Patient does not have such implants within their body that would require the use of modified imaging sequences.
4. No significant artifacts or other anomalies in the images in the calvaria volume.
5. All three image sets were complete and were not missing slices or otherwise cropped inconveniently.
6. Patient has a normal or close to normal bone structure in the skull.
 - (a) Decision made by the original treating doctor.

7. No other reasons to exclude any of the image sets or the patient from the study.

An example set of the original CT and ZTE images before any modifications is displayed below in Figure 2. It must be noted that, due to the wide range of CT HU values in the original images, it is possible that the true intensity distribution is not visualized correctly below.

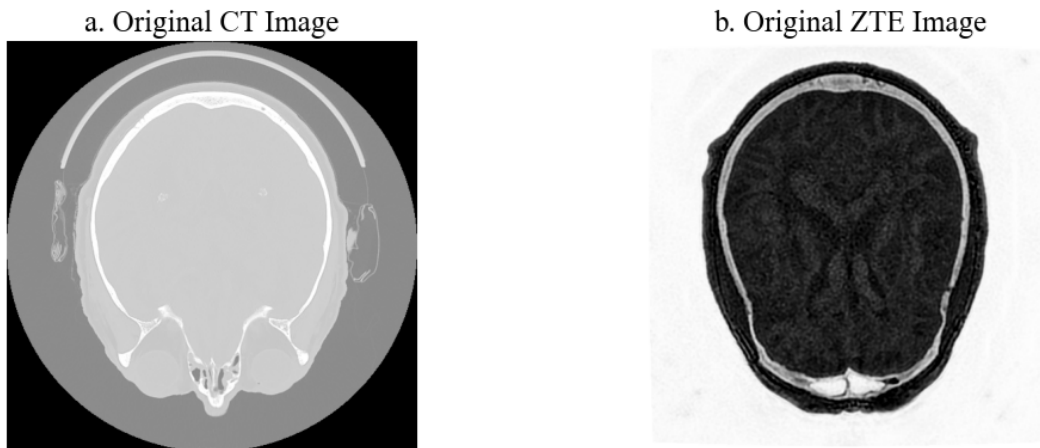


Figure 2: Raw images before processing. (a) Conventional CT and (b) normal ZTE images of one patient before any preprocessing or registration.

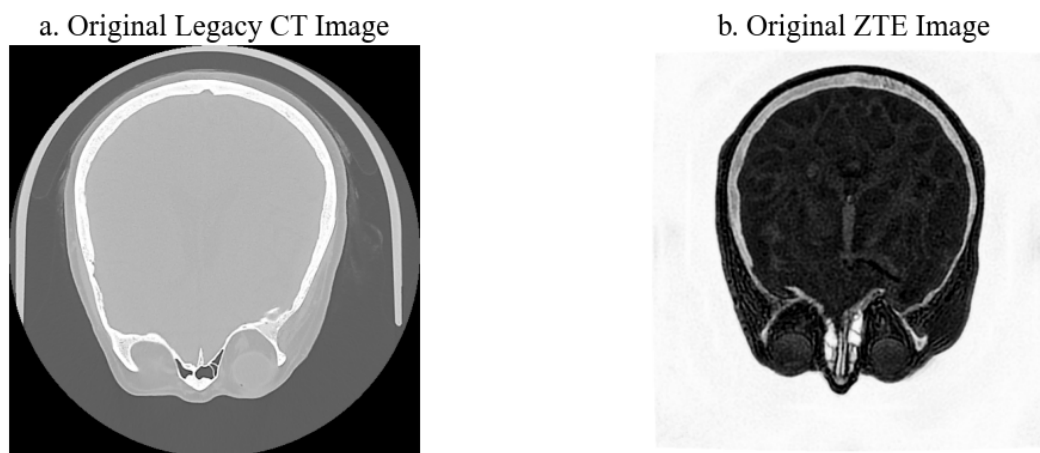


Figure 3: Raw images before processing. (a) Unconventional CT and (b) normal ZTE images of one patient before any preprocessing or registration.

The corresponding HU and intensity value distribution histograms from the raw images in Figure 2 are presented in Figure 4 below. The background voxels for all CT images have a HU value of -1000 , whereas the background voxels of the ZTE images varied. For this ZTE image set, the background voxels had an intensity value of 2000 . Both image sets resulted a maximum pixel amount peak in the background intensity value, as can be seen in Figure 4 below.

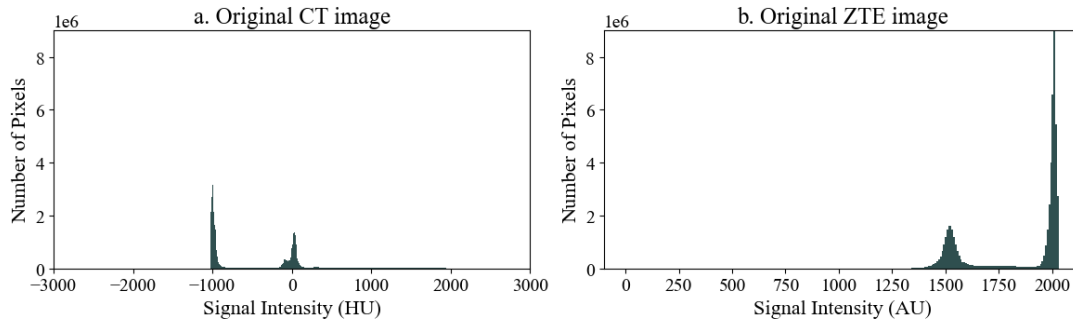


Figure 4: Intensity distribution histograms showing full intensity ranges. **(a)** Raw conventional CT HU value distribution and **(b)** ZTE intensity value distribution accordingly. The full background peaks are not displayed in order to keep the histogram scaled sufficiently for displaying purposes. Both histograms are from the images from the same patient.

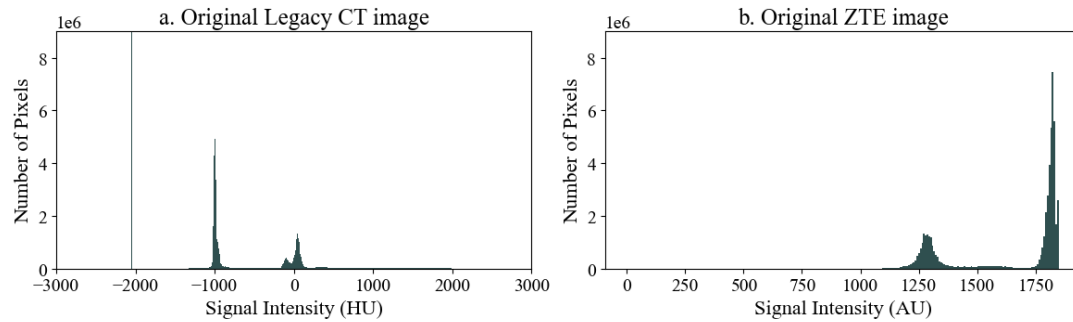


Figure 5: Intensity distribution histograms showing full intensity ranges. **(a)** Raw unconventional CT HU value distribution and **(b)** ZTE intensity value distribution accordingly. The full background peaks are not displayed in order to keep the histogram scaled sufficiently for displaying purposes. Both histograms are from the images from the same patient.

3.1.1 T1-weighted MR images

The anatomical T1-weighted MR images were used to transform the CT and the ZTE images into the same anatomical space. The anatomical MR imaging was performed with a GE SIGNA Premier 3T scanner, which is generally used to acquire anatomical images in TYKS. The magnetic resonance imaging was performed using the same imaging protocol as all HIFU treatment planning images.

The initial image matrix used for the anatomical T1-weighted MR images was 512 by 512, with 150 slices. The voxel size of most MR images was close to 0.5 mm by 0.5 mm, with 1.3 mm slice thickness. The details are provided in Table 1 below.

Table 1: Main imaging sequence parameters for the pretreatment T1-weighted MRIs.

| MRI Parameters | |
|---|---|
| MRI Scanner | GE SIGNA Premier 3T |
| FOV | 256 × 256 |
| Image matrix size | 512 × 512 |
| Number of slices | 150 |
| In-plane reconstructed pixel size (range) | [0.47–0.50] × [0.47–0.50] mm ² |
| Slice thickness | 1.3 mm |
| Sequence | 3D Sagittal T1-weighted Magnetization-Prepared Rapid Acquisition with Gradient Echo |

3.1.2 CT images

The CT imaging was performed with the top-grade GE Medical Systems Revolution Apex scanner, currently used in neuro-HIFU planning to calculate the SDR with the HIFU system.

The original image matrix of the CT images was 512 by 512, most of them having 200 slices. The voxel size was close to 0.5 mm by 0.5 mm, with 1.0 mm slice thickness. Some of the CT images were cropped to exclude areas with dental filling. These images were padded to size of 200 sliced in order to keep the image size stable and so that no stretching was caused to the image during the coregistration. This step is introduced in Section 4.2 in more detail. The details are provided in Table 2 below. The spatial resolution of the conventional CT images was the highest between the modalities.

Table 2: Main imaging parameters for the conventional pretreatment CTs currently in use.

| Parameters: Conventional CT | |
|---|---|
| CT Scanner | GE Medical Systems Revolution Apex |
| FOV | 256 × 256 |
| Image matrix size | 512 × 512 |
| Number of slices | 160–200 |
| In-plane reconstructed pixel size (range) | [0.44–0.56] × [0.44–0.56] mm ² |
| Slice thickness | 1 mm |
| Tube voltage | 120 kV |
| Mode | 3D |

In addition to the conventional CT images, $m = 6$ patients' unconventional CT images, and their corresponding anatomical and ZTE images were included in to the analysis. The unconventional CT images were acquired with previously used Toshiba Aquilion ONE CT scanner. The image matrix was 512 by 512, with 200 slices per

image, and the voxel size was close to the conventional CT images. However, the image quality was seemingly decreased compared to the conventional CT images. Details of the unconventional CT images are presented in Table 3 below.

Table 3: Main imaging sequence parameters for the pretreatment CTs previously in use.

| Parameters: Unconventional CT | |
|---|---|
| CT Scanner | Toshiba Aquilion ONE |
| FOV | 256 × 256 |
| Image matrix size | 512 × 512 |
| Number of slices | 200–211 |
| In-plane reconstructed pixel size (range) | [0.44–0.45] × [0.44–0.45] mm ² |
| Slice thickness | 1 mm |
| Tube voltage | 120 kV |
| Mode | 3D |

3.1.3 ZTE images

The zero echo time MR images were acquired with the same GE SIGNA Premier 3T scanner and during the same imaging session as the anatomical T1-weighted MR images. Therefore, the two image sets were as homogeneous as possible in terms of movement minimization between them.

The resolution of most ZTE images were comparable to the CT images; voxel size close to 0.5 mm by 0.5 mm, and slice thickness of 1 mm. The image matrix was 512 by 512, with 200 slices. There were no cropped ZTE images in the dataset, as ZTE is more robust against metal artifacts compared to the CT images. The pixel type of all three images for each patient was originally a 32-bit float. Details of the ZTE MR images are presented in Table 4 below.

Table 4: Main imaging sequence parameters for the ZTE images.

| ZTE Parameters | |
|-----------------------------------|-----------------------------|
| ZTE Scanner | GE SIGNA Premier 3T |
| FOV | 256 × 256 |
| Image matrix size | 512 × 512 |
| Number of slices | 200 |
| In-plane reconstructed pixel size | 0.46 × 0.46 mm ² |
| Slice thickness | 1 mm |
| Sequence | 3D Sagittal BONE |

3.1.4 Benchmark SDR

The SDR_{true} calculated by the Insightec HIFU system was available for all patients. It was used as the ground truth, against which the performance of the pipeline was validated and the usability of the derived ZTE-based values assessed. The true SDR of each patient was fetched and saved into a dataframe. As SDR greater than 0.35 was desired, each SDR_{true} value was checked before the patient and their data was selected to the study.

3.2 Artifacts

As the data used in this study were clinical data, almost all image sets contained some form of artifact. The most common sources of anomalies were amalgam filling and a patient having a slight abnormality in the bone formation of the skull. Other image quality affecting artifacts included movement during the image acquisition, and the region of interest (ROI) being slightly outside of the FOV in one image.

Out of the $n = 35$ patients, 20 of them had traces of amalgam in their teeth, making amalgam filling the most predominant source of artifact in the image data. Due to the prevalence of amalgam used in dental fillings, it was unfortunately not possible to exclude these patients from the study. The amalgam caused some of the CT image HU value ranges to spread significantly, leading to typical metal artifact and signal loss in the area. In addition, it caused some streaking artifacts in many CT images, especially in the dental region of the image. This issue was solved by segmenting the skull volumes for all patients. This skull mask creation also made the image size smaller, and therefore, the pipeline faster and lighter. It was ensured that no signal loss or metal artifacts were present on the skull masks prior to the SDR calculation.

The treating neurologist had diagnosed a few patients with distinct skull formations, such as an old trauma or benign overgrowth of the skull. For example, Benign hyperostosis frontalis had caused thickening of the inner table of the frontal bones of the skull, making the SDR of few patients naturally lower. It was initially decided that these patients were suitable for the HIFU treatment and their SDR was over the inclusion threshold of 0.35. Therefore, their images were included in the study as they represented the true subset of HIFU patients.

4 Research methods

This study aims to compare the SDR_{ZTE} values, derived from ZTE MR images, against the SDR_{true} , and CT-derived SDR_{CT} values to evaluate whether ZTE can be used for skull attenuation estimation and thus, for HIFU pretreatment planning. To facilitate this, a semi-automatic pipeline was developed for image registration, segmentation, and intensity-based skull density ratio calculation, replicating the methodology used in SDR_{true} calculation process performed by the Insightec neuro-HIFU system. The developed algorithm was first validated by calculating the SDR_{CT} values from the conventional CT images and then comparing them against the benchmark SDR_{true} values. After the validation reached sufficient accuracy, the algorithm was used to calculate the SDR_{CT} values from the unconventional CT images and SDR_{ZTE} values from the ZTE images. In addition, the skull thicknesses were calculated from the original conventional CT images.

After the SDR calculation was done from all images, the SDR_{ZTE} values were compared against the corresponding SDR_{CT} values, as well as to the ground truth SDR_{true} values provided by the Insightec HIFU system, to evaluate the clinical suitability of SDR_{ZTE} estimation.

Section 4.1 first outlines the overall study design and introduces the structure of the semi-automatic pipeline developed for this Thesis, including the introduction of the helper scripts used to support registration, visualization, and the graphical user interface for Jupyter Notebooks. After the preprocessing steps to obtain images with high mutual information for the registration purposes are introduced in Section 4.2, the methods for coregistering the patients' CT and ZTE images to the space of their own anatomical T1-weighted MR images are presented in detail in Section 4.3. As the obtained registration transformation was ultimately applied to minimally processed images, the final preprocessing of the images is presented in Section 4.4. After the images were processed accordingly, the skull mask was segmented in 3D Slicer to create the calvaria volume used in the SDR calculation as presented in Section 4.5. The skull density ratio is finally calculated in Section 4.6 using a set of $n = 1093$ spherically distributed lines placed inside the skull mask, spreading from the origin through the calvaria. The SDR algorithm used peak detection modalities to distinguish the global maximum and the local minimum along the obtained intensity profiles. Once the sufficient minimum and maximum were detected, the SDR was calculated with Equation 2 given in Section 2.3.2. Lastly, before the correlation analysis of the SDR values are presented in Section 4.8, the skull thickness estimation is outlined in Section 4.7.

4.1 Pipeline

The basis of the pipeline was built on existing mathematical formulas for SDR calculation found in literature, introduced by Equation 2 in Section 2.3.2, and based on a discussion with Kevin Tsai and Itay Rachmilevitch from Insightec [34, 36]. Since each patient's images were grouped into sets, each set was processed through the pipeline as a single unit separately for each patient. A simplified illustration of the

analysis pipeline design is presented below.

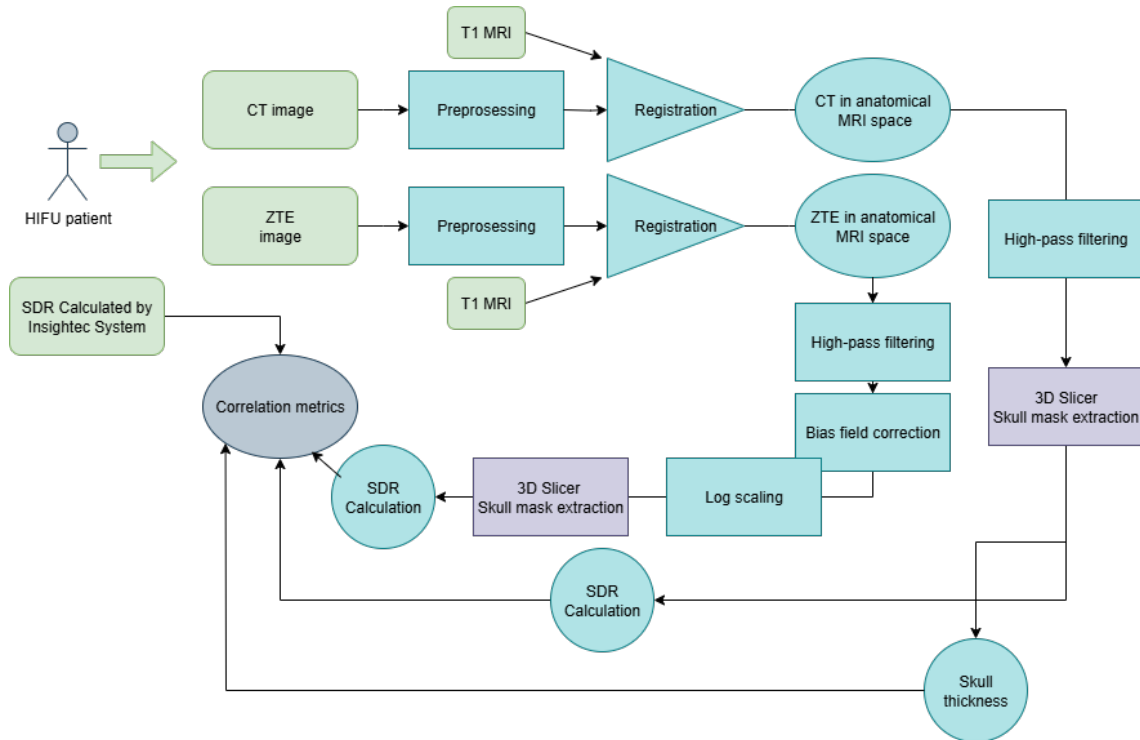


Figure 6: Simplified illustration of the study pipeline design. Blue and gray steps are performed in a Jupyter Notebook and purple steps in the 3D Slicer. Green data types are collected from a HIFU patient during the clinical planning phase of the treatment.

The green patient data presented in Figure 6 was fetched from the Philips Picture Archiving and Communication System (PACS) used in TYKS. Since the original SDR algorithms used by Insightec are proprietary, a custom SDR processing pipeline was developed using Jupyter Notebooks with Python for numerical computing and 3D Slicer for visualization and manual ROI segmentation [43, 44]. The Jupyter Notebook pipeline, marked as blue in Figure 6, was used for the data preprocessing and coregistration steps and eventually, for the intensity-based SDR calculation, and final correlation metrics evaluation marked as gray. After the registration, the registered CT and ZTE images entered the skull bone extraction step performed in 3D Slicer, marked as purple in Figure 6, where a mask of the desired skull volume was created. The ROI was extracted, and the SDR calculated. Finally, the correlation metrics were evaluated between the calculated SDRs, as well as for the SDRs and skull thicknesses.

As image analysis requires a moderate amount of calculation power from the computer when run locally with a large set of images, the analysis was divided into multiple parts. The entire analysis pipeline was optimized as much as possible to ensure semi-automatic structure and user experience. The contents of the Notebooks are presented in more detail in Sections 4.2–4.8. The whole Jupyter Notebook structure is presented in detail in Table A1 of Appendix A for future reference.

4.1.1 Helper scripts

Open source helper scripts were used to support the pipeline graphical user interface (GUI) and to monitor the efficiency of the coregistration convergence. The supportive classes were found on GitHub, and it was ensured that permission for research use was given.

For registration visualization purposes, a GUI script provided by Simple Insight Toolkit (SimpleITK) Tutorials was used [45]. The `gui.py` script allows the user to create a linked cursor approach to ensure the fixed image points are mapped correctly to the moving image domain after the registration. The GUI allows the user to select the intensity window of the images displayed, helping in the window selection and filtering approaches. Most importantly, the GUI can be used to view the images before and after modifications have been made.

SimpleITK Tutorials `registration_gui.py` was used for tracking the registration minimum convergence between the image spaces [46]. The registration GUI monitors the convergence of the registration and plots it as the iterations proceed. Therefore, the user is able to visualize if the registration reached a stable global minimum. In addition, the GUI class prints the end criteria of the registration, providing important information for the user.

4.2 Preprocessing

The goal of the image preprocessing was to ensure patient privacy, comparability between the imaging modalities and image sizes, and that each image was in the correct coordinate system. Preprocessing was performed in two phases following the anonymization and format conversion: first, on the images used to compute the registration transformation matrix; and second, on the original images after they were registered using the obtained matrix. First, the images used to find the transformation matrix were preprocessed so that the mutual information between the images and the anatomical MRI would be as high as possible, in order to find the most sufficient registration between them. This included mainly intensity rendering, but also size padding and resampling.

The same padding and resampling was eventually done to the original but registered images, later used in the segmentation, but the filtering scheme used was different. After each preprocessing step, image quality and intensity distribution was reviewed, as preprocessing might affect the intensity distribution and other quality aspects. The aim was to keep the image quality as stable as possible, in order to remain the true intensity distribution of each image. The final image postprocessing, done after the registration, is introduced in Section 4.4.

4.2.1 Anonymization

All MR, CT, and ZTE image sets for each patient were retrieved from PACS. At the same time, the baseline SDR_{true} values calculated by the Insightec system prior the treatment were saved. In order to keep patient information minimal, all image

sets were anonymized before downloading the corresponding Digital Imaging and Communications in Medicine (DICOM) image directories. To keep all patient details linkable, the following anonymization protocol was used:

1. Each patient with the conventional image set was assigned an unique three-character number with leading zeros from 001 to 029:
 - (a) The anatomical MR image set was named as MRI_00x
 - (b) The conventional CT image set was named as CT_00x
 - (c) The ZTE image set was named as ZTE_00x
2. The image sets with CT scans acquired with the unconventional, older generation scanner followed the same idea, but an ending was added:
 - (a) The anatomical MR image set was named as MRI_00x_un
 - (b) The unconventional CT image set was named as CT_00x_un
 - (c) The ZTE image set was named as ZTE_00x_un

A dataframe including the patient's number, Insightec SDR_{true} , sex, age, and additional notes about possible artifacts was combined.

4.2.2 Format conversion

The image file structures for each patient were retrieved and downloaded to the local Jupyter Notebook setup. The data were originally packed into two DICOM directories; one of which contained the MRI and ZTE data, and the other containing the CT data for each patient. The datasets were converted into a Neuroimaging Informatics Technology Initiative (NIfTI) format as NIfTI is compatible with most data analysis tools and packages.

The first Jupyter Notebook in the analysis pipeline was designed to perform the DICOM to NIfTI conversion efficiently and to inspect the metadata of the image sets. It utilizes a Python `dicom2nifti` package, as it is compatible with CT and MR format conversions. The created script loops through every provided DICOM file in the directories and confirms that it is indeed a DICOM entry. After the file type confirmation, it prints the DICOMs header and shape, so that the user can confirm that the directory is correctly combined and imported from the PACS. After the sanity checks, the code retrieves the needed image sets and names the output NIfTI files as described in Section 4.2.1.

The Python function used for the CT image conversion was `series_to_nifti` as each CT DICOM directory only contained one CT set for each patient, as displayed below.

```
dicom2nifti.dicom_series_to_nifti(
    entry, output, reorient_nifti=True)
```

For the ZTE and MR image conversions, the Python `convert_directory` function was used, as the ZTE and MR image sets were in the same DICOM structure.

```
dicom2nifti.convert_directory(
    entry, output, compression=False, reorient=True)
```

The compression was selected to be `False` as zip files were not needed in the analysis. However the `reorient` variable was kept `True`, in order to keep the image axes *LAS* (left, anterior, superior) oriented.

4.2.3 Verification

Although a primary review was done on each image set during the manual PACS export, a metadata sanity check of each image set was displayed during the file type conversion. The script confirmed that the image matrix size and the used imaging modality for each image set were as expected, to avoid images acquired with other scanners or with different FOVs than those presented in Chapter 3.

Therefore, the image set passed the sanity check if the medical imaging machine name was correct, and if all image matrix sizes were 512 by 512, with varying slice thicknesses. In addition, the verification script saved the origin, spacing, direction, pixel type, and number of pixel components to evaluate the metadata of each image before and after the later modification and registration.

4.2.4 Preparation

Before registration, the original CT HU values and ZTE image window levels and window widths were evaluated with a SimpleITK MinimumMaximum filter. In addition, the HU value and ZTE intensity value histograms were printed for each image pair to evaluate the distribution in each image. The information obtained from this step was first used in the mutual information maximization filtering, and eventually in the high-pass filtering threshold of the registered images. Therefore, all CT and ZTE image intensity values were filtered and resampled prior the registration in order to enhance the mutual information with the MR images and thus, to find the most accurate registration transformation. However, these preprocessed images were not resampled with the final transformation, but were only used to find the optimal transformation between the images.

In addition to the intensity rendering, the images were resampled so that they would occupy the same physical space. The MR images were resampled to 512 by 512 grid with 200 slices, with voxel size of $0.5 \times 0.5 \times 1 \text{ mm}^3$. The origin and direction were kept original. Upsampling the MRI ensured that the images were of the same physical size and thus, ensured a high quality registration.

As some CT images had only 150 to 170 slices due to cropping of amalgam filling out of the image, the CT images were padded to the 200 slice amount by filling the bottom of the image matrix with background voxels with HU values of -1000 . This was done to ensure that the image size is the same between the modalities, and thus, to ensure that the CT images were not stretched due to the different sizing. Therefore,

after the MRI upsampling and CT image missing slice padding, all images had the same matrix size of 512 by 512 grid with 200 slices.

4.3 Coregistration

Once the MR images were upsampled and the CT and ZTE images filtered to ensure that the mutual information was as high as possible, the registration transformation matrix was calculated using the developed pipeline. The goal of the registration was to find an affine transformation matrix that maps the points from the fixed, MR, image volume to the corresponding points of the moving CT and ZTE image volumes.

This Section presents the registration algorithm, virtual image domain, and introduces the used parameters, including the initialization, similarity metric, interpolators, and optimizer. From here on, fixed image refers to the anatomical T1-weighted MR image of the patient, and the moving images refer to the CT and ZTE images of the patient.

4.3.1 Virtual image domain

As the analysis pipeline was designed to be used locally without the aid of external servers, the image registration was performed via a virtual image domain, ITKv4, provided by Insight Toolkit, instead of directly mapping the moving image to the space of the fixed image. The virtual image domain allows the user to examine the registration progress before the final transformation is resampled and saved by the pipeline. Therefore, the image was saved only if the user is pleased with the convergence of the registration iteration, differing from a traditional registration, where the image is resampled and saved instantly. In addition, only the moving transformation is optimized. Therefore, the use of the virtual image domain optimizes the use of memory and calculation power.

An optimizer, a similarity metric, and an interpolator were chosen for the registration pipeline. The virtual image domain code follows the GitHub example of SimpleITK tutorials with sufficient modifications [47, 48]. The complete registration code can be found in Appendix B.

4.3.2 Initialization

The initialization of the fixed and moving image volumes is crucial, as it determines where the registration iteration is started. If the distance to the desired registration result is too long, the registration might converge to a local minimum instead of the desired global minimum. The runtime and the outcome of the registration are therefore highly dependent on the transform initialization.

A centered transform initializer was selected, as the centers of all three clinical images were expected to be approximately close to each other, providing a short distance to the desired registration. The centered transform initializer provides a translation based on aligning their geometric centers and starts the registration from

there. Therefore, the Insight Toolkit's centered transform initializer geometry filter was used to prealign the two image volumes. The utilized transform initialization function is displayed below.

```
initial_transform=sitk.CenteredTransformInitializer(
    fixed_image,moving_image,sitk.AffineTransform(3),
    sitk.CenteredTransformInitializerFilter.GEOMETRY)
```

4.3.3 Similarity metric

An affine transformation was selected as the registration paradigm is multimodal, but the registration is performed between the patient's own images. Affine registration has 12 degrees of freedom: translation, rotation, shearing, and scaling in all three directions. This means that the transformation can move, rotate, scale, and distort the image, but preserves the parallelism.

Registration of the two image volumes was performed using Matte's mutual information (MMI) approach, which maximizes the mutual information between the two volumes by minimizing the cost function. The MMI is not solely intensity-dependent, which is important in this registration, where the intensity distributions of the images are different. The optimizer converges based on a continuous and differentiable function of the registration parameters, implemented with Partzen windows [49]. The method applies different order B-spline kernels to calculate the probability densities between the fixed and moving images [49]. The MMI algorithm ensures high efficiency by using the same set of sampled pixel locations throughout the optimization, rather than resampling each time. Thus, MMI was selected to calculate the mutual information between the fixed and moving images for its decent accuracy, popularity in similar tasks, and high efficiency.

The percentage of samples used to calculate the probability density estimates was set to 1 percent, and the number of histograms used to compute the entropy to 50. The sampling strategy was set to be random. The downsampling and Gaussian smoothing parameters selected define the image pyramid used. In the algorithm, the original image is first smoothed, and possible aliasing is tackled by removing high-frequency components. After that, the image is resampled based on the set shrinking factors. Utilizing the image pyramid scheme makes the registration more robust to initial misalignments, and additionally, often expedites the process [49].

A high mutual information between the fixed and the moving image indicates that there is less entropy and thus less uncertainty between the two registered images, suggesting that a global minimum has been reached between the two image volumes. The SimpleITK MattesMutualInformation returns the negative mutual information value displayed in Table 5 in Chapter 5. It should be noted that for the metric value, a lower similarity metric is better.

4.3.4 Interpolators

Two interpolators were selected, one for finding the transformation matrix with the enhanced images and one for resampling the original moving image into the fixed image's space. The interpolator defines how the image is resampled from one coordinate system to another. The resampling process requires estimation, and thus, the interpolator determines how pixel values are estimated in the resampling and transformation. The selected interpolator for finding the transformation matrix was the SimpleITK linear interpolator, as it was a good compromise between accuracy and sufficient computational efficiency. The SimpleITK linear interpolator assumes a linear relationship between the pixel values. A nearest neighbor interpolator was chosen for the final image resampling, as it preserves the intensity dependency by interpolating the pixel values based on the nearest pixel, therefore maintaining the true intensity distribution as much as possible.

4.3.5 Optimizer

The selected optimizer determines how the next optimization step is performed by iteratively adjusting the transformation to converge on a local minimum. The selected optimizer was a SimpleITK Gradient Descent optimizer that performs the steps by following a predetermined gradient function. The selected learning rate was one, and the number of iterations was set to 1000, although sufficient registrations were achieved around 9-20 iterations. The convergence minimum value was set to 10^{-6} and the convergence window size was kept at the default 10.

4.3.6 Verification

The iteration graph, convergence passing criteria, and mutual information metric value were plotted to assess the convergence of the transformation matrix iteration. A mutual information metric value was calculated and saved to ensure that the mutual information between the registered image and the MR image was sufficient. The registration transformation matrix was saved if the mutual information was close to -0.3 for CT images with a padded volume and over -0.5 for CT images without the padded volume, as the padded volume impacts the amount of mutual information that can be found between the images. A metric value close to -0.6 was selected for all ZTE images, as they had more mutual information with the MR images naturally, due to them being acquired in the same setting. The convergence stopping criteria of each iteration was printed and evaluated, to ensure that the minimum was reached. The correctness of all registrations was visually inspected using alpha blending and checkerboard image filtering to overlay the two volumes: the original T1-weighted anatomical MR image and the CT and ZTE images transformed into the MR space separately.

a. Registered and filtered CT image



b. Registered and filtered ZTE image

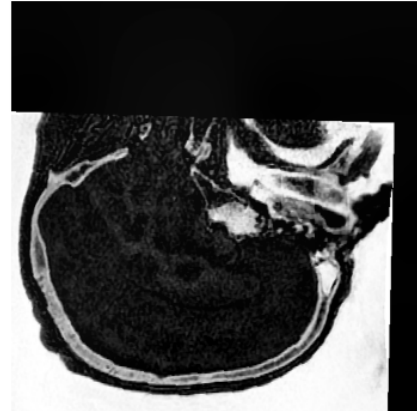
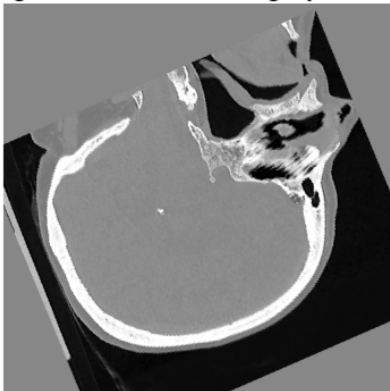


Figure 7: Registered conventional CT and ZTE image in the anatomical MRI space. (a) Conventional CT and the corresponding (b) ZTE image after preprocessing, registration and resampling.

a. Registered and filtered legacy CT image



b. Registered and filtered ZTE image

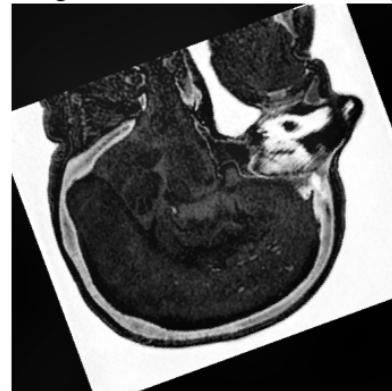


Figure 8: Registered unconventional CT and ZTE image in the anatomical MRI space. (a) Unconventional CT and the corresponding (b) ZTE image after preprocessing, registration, and resampling.

If the registration passed the aforementioned checks with a suitable margin, and if the convergence stopping condition was sufficient, the coregistered CT and ZTE images were resampled with the acquired transformation matrices. The registered image was resampled to the MR space with its original voxel size to avoid partial volume effects in the segmentation as much as possible. All metadata were evaluated again after the registration and resampling to ensure that the image sizing and spacing were as intended. The metadata of the registered moving images presented that the origin of the registered images was the same as that of the original MR image. The images' pixel types were kept as 32-bit float throughout the analysis to avoid introducing error to the intensity distribution.

4.4 Image postprocessing

The image intensity enhancement steps performed in Section 2.2, before the registration transformation calculation, were done to improve the accuracy of the acquired transformation matrix. As the SDR and skull thickness calculation rely on the intensities, all image processing should preserve the true intensity distribution of the images as much as possible. Therefore, the final transformation matrix, calculated based on the enhanced images, was applied to the original, unfiltered images. The decisive preprocessing of the final images was then performed after resampling the images with the acquired transformation matrix to avoid artifacts in the intensity distribution caused by interpolation.

First, high-pass filtering was applied to the registered CT and ZTE images in order to exclude excess noise and, most importantly, the signal loss values caused by the amalgam filling present in most images. The high-pass filtering was applied so that the original and skull-relevant intensity distribution was preserved as much as possible. Therefore, the filtering threshold for the CT images was set to -1100 HU. The selected HU value was close to the background-air boundary, making the signal loss areas the same HU as the background. The threshold for high-pass filtering of the ZTE images varied, as the intensity distribution value ranges were not constant, meaning that the intensity peaks appeared at very different intensities, unlike in the case of the CT images. The threshold selected for the ZTE images was decided via the lower intensity peak location for each image separately. This threshold presented the same intensity as used for the CT image filtering. Most of the ZTE filtering thresholds were between 1100–1700, with occasional smaller and larger values, depending on the peak values on the distribution. Importantly, the aim of the filtering was not to interfere with any intensities within the bone mask. This filtering step was essential for improving the accuracy of the later segmentation step, and in order to delimit the intensity distributions of all images to sufficient ranges and their peaks to the same locations of the histograms.

Once the CT images were registered and high-pass filtered, they were exported to the 3D Slicer directory for segmentation. Before saving the registered and high-pass filtered ZTE images to 3D Slicer for skull segmentation, a bias field correction was applied to them, using the N4 Bias Field Correction algorithm [50]. The low-frequency bias field signal is present in all MR images, and it blurs the MR image by reducing the high-frequency information [51]. The bias field artifact can be caused by inhomogeneities in the static magnetic field, imperfections in the RF transmit and receive coils, and by other field or coil inhomogeneities [52]. As the present bias field signal can alternate the intensity values of the same tissue, resulting in them having different intensities, its presence would greatly interfere with the performance of the threshold-based segmentation algorithm. Given the computational cost of the bias field correction algorithm, it was applied only to the skull region using a binary mask created from the skull area.

Finally, after the bias field correction and high-pass filtering of the ZTE images, their intensity values were rescaled using a base ten logarithm to replicate an intensity profile close to the CT images, as described by Caballero and colleagues and Wiesinger

and colleagues [5, 10]. This intensity rescaling normalized the intensities to a 0–1 range, and enhanced the contrast between low and high-intensity regions, crucial to the naturally lower contrast ZTE images. Once the ZTE images were processed, they were saved and exported to the 3D Slicer directory.

4.5 Skull mask creation

To pass only the calvaria skull volume to the intensity-based SDR calculation algorithm, a ROI selection and skull volume segmentation were performed for the registered images. For this purpose, a skull mask of the calvaria was extracted from the CT and ZTE images using threshold-based segmentation in 3D Slicer.

4.5.1 Platform

As the analysis required complex anatomical segmentation of fine bone structures, a good visualization tool was needed. 3D slicer is an open source, C++, Python, and Qt-based software developed for image analysis and visualization purposes [53]. Over 12,000 studies have utilized 3D slicer since 2021 [44]. It was selected for segmentation purposes, as it can be run locally, although it does require some computing power, CPUs and GPUs, from the computer.

4.5.2 Region of interest

Before the bone segmentation was performed, a suitable ROI was cropped from the CT and ZTE images to ensure that the created volumes are comparable. Cropping also excluded any source of error caused by segmentation outside of the ROI tissue. The calvaria was manually cropped following the line from the upper orbit to the genu of the corpus callosum as presented in Figure 9. This was selected, as it is relatively easy to identify from the MR images of all patients, compared to the conventionally used AC–PC line. This area of the calvaria receives the passing HIFU beams during the treatment, and thus, the SDR was calculated from this skull volume.

The ROI was extracted in 3D Slicer by first creating the ROI selection area using the landmarks in the T1-weighted MR image, separately for each patient, as the anatomy of each patient was different. A slight negative sagittal rotation transformation was applied to the selection area to align it with the line from the upper orbit to the genu of the corpus callosum. All three slice orientations were examined to confirm that the ROI selection box was in the correct position. Once the size of the selection area was adjusted, the volume cropping module was used to crop the ROI volume from the CT and the ZTE images of the patient separately. As the CT and ZTE images were registered into the MR space, the created volumes included the same skull volume and landmarks. The created calvaria 3D volumes proceeded into the segmentation phase of the study.

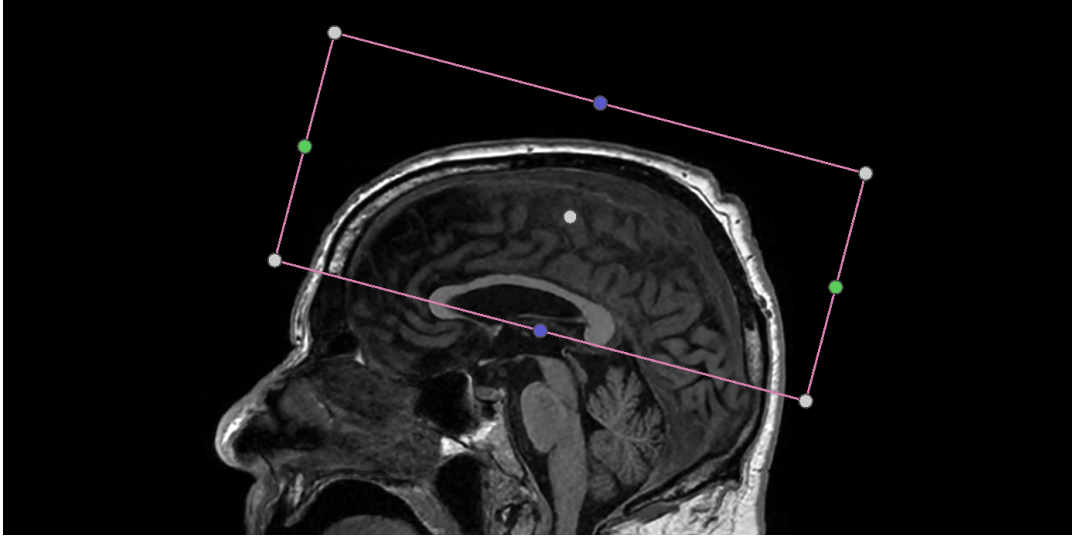


Figure 9: Region of interest inside the pink selection area. The bottom of the selection area follows the line from the upper orbit to the genu of the corpus callosum. The skull volume inside the ROI selection area was cropped and processed into the segmentation.

4.5.3 Segmentation protocol

After the ROI was selected and cropped, the segmentation masks were created separately from the CT and ZTE volumes with an intensity threshold approach. It must be noted that the eventual intensity-based SDR algorithm seeks a local minimum between two maxima. Therefore, the skull mask threshold was not selected too high to conserve the cortical bone's true edges as much as possible.

The threshold was selected based on the image's intensity histograms to separate the background and the cortical bone using 3D Slicer's segmentation editor module. Once the suitable threshold was found, the segmentation was applied to the calvaria volume, after which only the largest segmentation was selected. A Surface Wrap Solidify extension, provided by 3D Slicer modules, was used to fill in the holes within the segmentation volume, caused by the lower intensity trabecular bone [54]. The Surface Wrap Solidify module creates a solid segment using shrinkwrapping, projection, and solidification algorithms. The extension's carve holes parameter was set to 10 mm, oversampling rate to 1.5 times, the number of iterations to 6, and the smoothing parameter was set to zero.

After the solid segmentation label map was created, it was used to mask out the skull volume. The results of the segmented volume were visualized using a 3D view. The segmentation label map creation and volume masking were performed separately for the CT and the ZTE images to preserve their unique interface properties. An example of the created CT and ZTE calvaria volumes for one patient is presented below in Figures 10 and 11 accordingly.

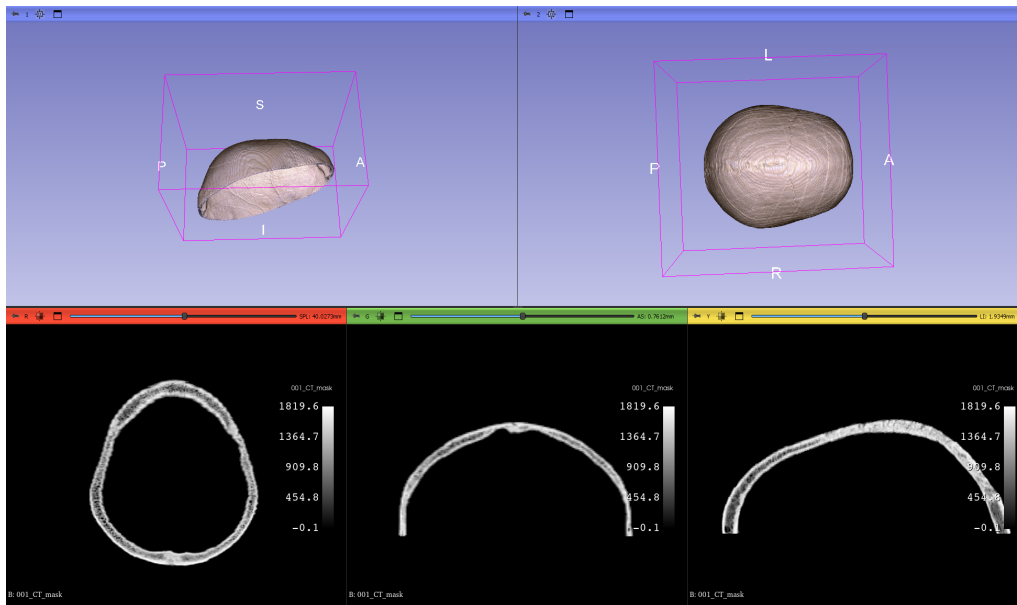


Figure 10: An example of the created 3D calvaria volume of one CT image on the upper part of the Figure. Distal, dorsal, and medial views in the lower part, respectively.

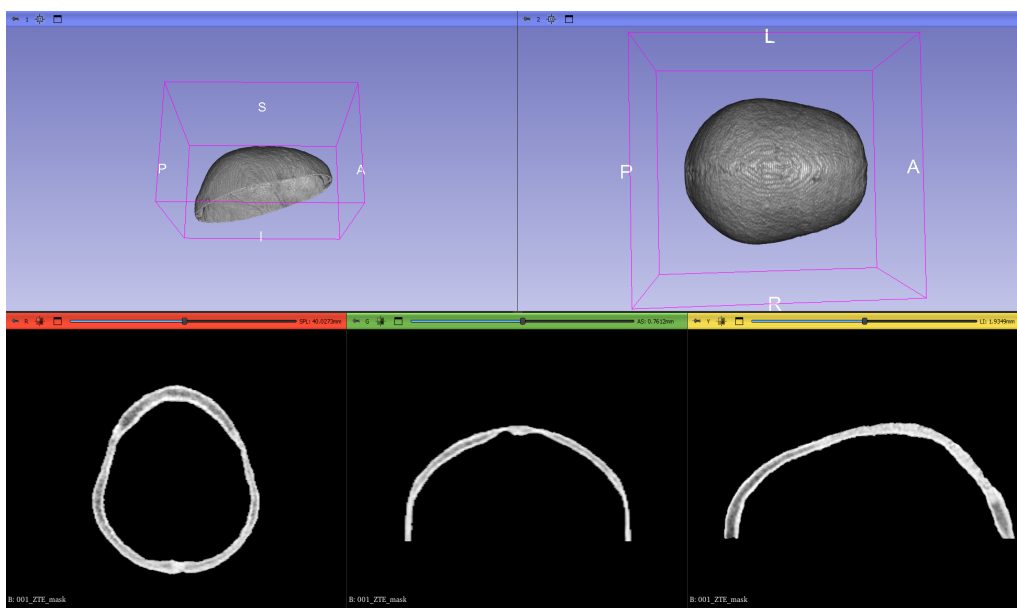


Figure 11: An example of the created 3D calvaria volume of one ZTE image of the same patient on the upper part of the Figure. Distal, dorsal, and medial views in the lower part, respectively.

The segmentation of the unconventional CT images followed the same protocol. An example of segmentation of an unconventional CT image is displayed below in [Figure 12](#).

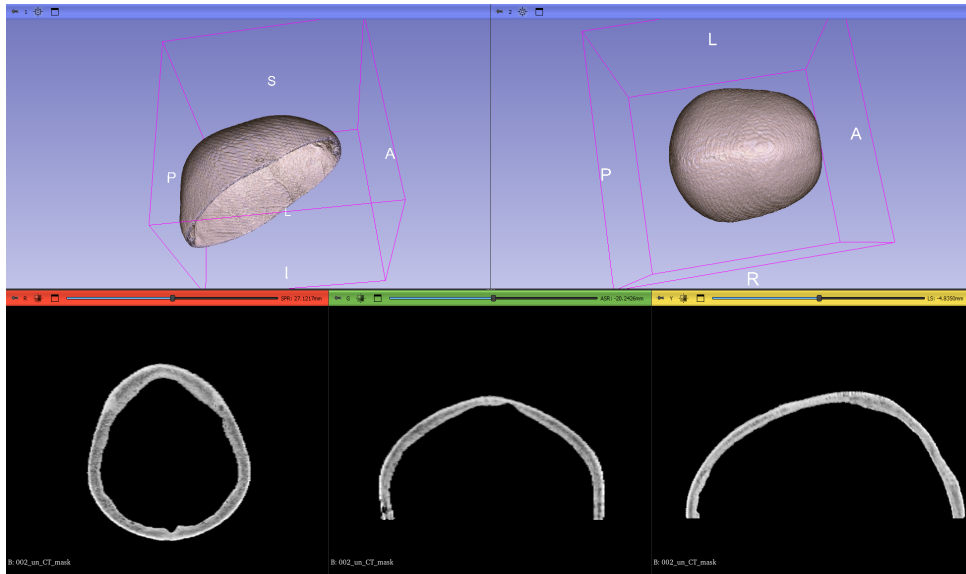


Figure 12: An example of the created 3D calvaria mask volume of one unconventional CT image. Distal, dorsal, and medial views in the lower part, respectively.

Figures 10, 11, and 12 display the intensity and contrast characteristics and their differences between the methods. As no smoothing was applied to maintain the true intensity distribution, the pixel-wise segmentation can be seen on the boundaries of the skull caps. Figures 10 and 11 are from the same patient, and the CT cap created from an unconventional CT scan in Figure 12 is naturally from a different patient, as there were no patients that would have had both the conventional and the unconventional CT scans available. It can be seen from the Figures how the true landmarks of the skulls were preserved during the registration and segmentation although the image quality is always affected during resampling.

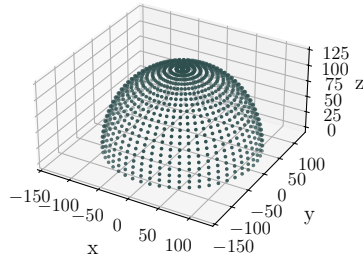
4.6 SDR calculation

Once the CT and ZTE bone masks were segmented, they were imported to the SDR calculation Notebook. The SDR calculation script includes the creation of a spherical line model to map the intensity profiles through the calvaria, the coordinate conversions, peak detection, and eventually, the SDR calculation.

4.6.1 Hemispherical line model

To calculate the local minimum and global maximum intensities along each beam, a line model was created to model the beam geometry from the transducer to the intracranial target. The algorithm first creates 1093 lines in spherical coordinates. Each line has one end in the intracranial origin close to the VIM, and the other end on an extracranial spherical surface, with a radius of 12 cm. The created lines are separated with equal angles horizontally and vertically. The hemispherical line model is presented in Figure 13 below, with two different visualizations.

a. Hemisphere with points



b. Hemisphere with lines

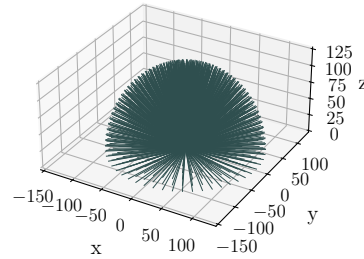


Figure 13: The hemispherical line model with two different visualizations. **(a)** With dots on end coordinates and **(b)** with the connected lines reflecting the actual usage.

The algorithm labels each line with a unique name from L1 to L1093, and saves the start and end coordinates of each line to a JavaScript Object Notation (JSON) file. The JSON file is readable in Jupyter Notebooks, and it has the needed schema to be opened in 3D Slicer for visualization.

As 3D Slicer uses mainly *RAS* (right, anterior, superior) and *LPS* (left, posterior, superior) coordinate systems, and Jupyter Notebooks uses the classical *xyz* Cartesian coordinate system, the skull volume was rotated and its origin updated to ensure that the skull volume and the line model are aligned sufficiently in the world coordinate system. The overlaid line model and skull cap with the aligned coordinate systems are displayed below in Figure 14 from two different directions. The origin of the line model is placed in the middle of the *xy*-plane of the skull, where the VIM is roughly located.

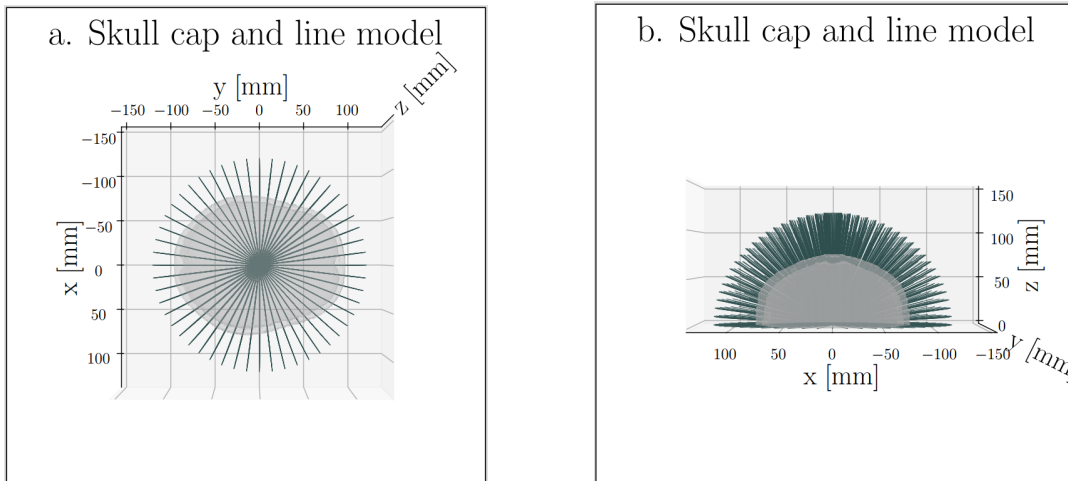


Figure 14: Hemispherical line model and the segmented calvaria. Overlay **(a)** from the superior view and **(b)** from the anterior view, displaying the alignment.

The number of lines, 1093, is slightly more than the conventional 1024 elements in an annular sectored phase array of a regular HIFU helmet [18]. Increasing the number of lines did not change the resulting SDR significantly, but increased the calculation time slightly.

4.6.2 Peak detection

The basis of the SDR calculation algorithm lies in Equation 4, which is described in more detail in Section 2.3.2:

$$SS = \frac{\sum_{k=1}^P \min(I_k) / \max(I_k)}{P}, \quad (4)$$

where P indicates the 1093 beams from the transducer, $\min(I_k)$ is the minimum and $\max(I_k)$ is the maximum skull intensity along k^{th} beam, respectively [8].

The algorithm utilizes multiple peak detection modalities from SciPy signal processing Python packages to distinguish the sufficient values from the profile [55]. The intensity profile along each line was sampled with 500 samples perpendicular to the skull volume, along its thickness. It was expected that most line profiles through the skull cap would have two maxima and one global minimum between them. This assumption is based on the general layered structure of the skull, where lower intensity trabecular bone is sandwiched between two higher intensity cortical bone tables. Therefore, the algorithm primarily seeks a local minimum between two maxima. However, there can be multiple local maxima and minima along the line profile. Thus, the algorithm first performs value selection for the latter SDR calculation, and ensures, that the selected values are within the true skull mask boundaries. An ideal skull intensity profile through a skull volume is presented in Figure 15 below.

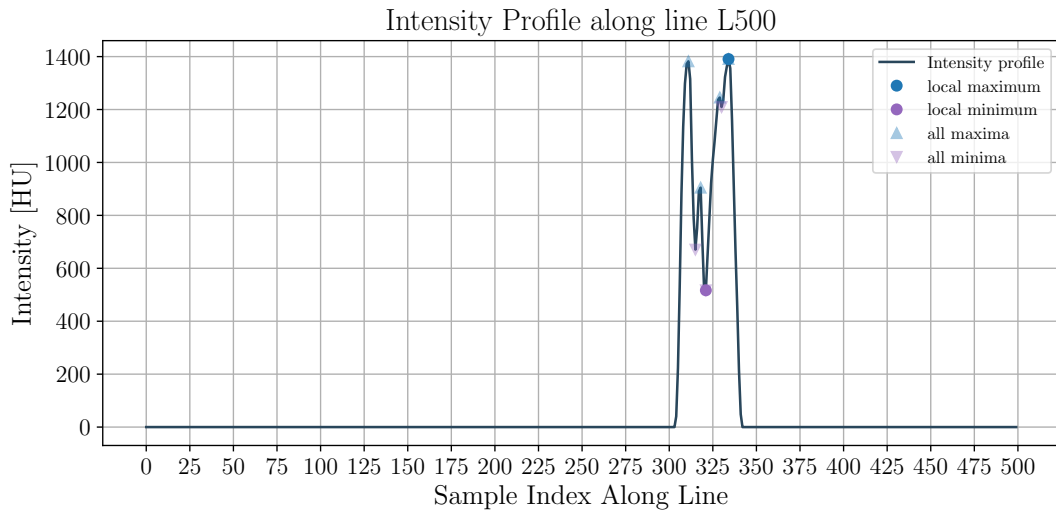


Figure 15: Intensity profile along line L500. All extrema are marked with triangles, but only the smallest and largest of them are marked as circles and selected for SDR calculation.

However, as the skull structure is not uniform, the expected local minimum and a global maximum are not always present along the line, as in the ideal circumstances. Therefore, the algorithm also takes into account the intensity profiles with more unique properties. These include parts of the skull, where only dense and thus high-intensity cortical bone is present, or where the thickness of the trabecular bone is less than the voxel size. In such scenarios, only one maximum is present along the profile, and the function has no distinct minima within the skull mask. Despite the missing distinct local minimum, the intensity profile is not constant within the cortical bone region. In these scenarios, the algorithm saves the global maximum of the profile, and for the minimum, it selects the minimum value, which truly lies within the skull mask, but is not due to the partial volume effect in the skull and background boundary. Thus, the algorithm selects the smallest minimum value only if it lies no closer than a few samples from the skull-background interface, to avoid a minimum in the partial volume effect area.

If there are no minimum values within the true skull mask volume, meaning that the whole skull intensity profile is constant, the algorithm saves the constant value as the minimum and as the maximum. This scenario might be present if the skull thickness along the line is very thin, and thus, only few samples remain between the margins.

Once each line has been sampled and the intensity profile's minimum and maximum detected and saved to a dataframe, the algorithm calculates the SDR as the mean ratio of intensity minima and maxima from all lines. The calculated SDR is then saved into a dataframe, and imported to the correlation analysis Notebook. The resulting SDR_{CT} and SDR_{ZTE} values from all images of each patient are presented in Section 5.2.

4.6.3 Algorithm testing

The SDR calculation algorithm was first tested with the conventional CT images, used originally to calculate the SDR_{true} by the Insightec system. Once the pipeline detected all minima and maxima with sufficient marginal from the CT images, the same calculation was done to all 70 CT and ZTE skull volumes separately. It was ensured that the patient's CT and ZTE volumes are placed in the same location, and thus, that they had the same origin.

Due to general interest, the SDR calculation algorithm was also tested with a small subset ($m = 6$) of unconventional CT images. The whole analysis followed the same pipeline as for the conventional CTs, including the ZTE images and T1-weighted MR images. The benchmark SDR_{true} values were also collected from these patients.

Due to the small sample size of the data, no statistically significant conclusions can be drawn, but the SDR values are reported in a similar manner as for the dataset of $n = 29$ conventional images. The subset images were not included in the same batch as the conventional images, to keep the original dataset homogeneous.

4.7 Skull thickness estimation

Previous studies generally recognize that the SDR is not a sufficient standalone measure, although being the most important one, when assessing the skull attenuation characteristics in terms of neuro-HIFU optimization [24]. Although, the skull thickness of the patient does not necessarily correlate with the SDR, it does play a role in the HIFU treatment success and efficiency of the ultrasound energy transfer. This is due to the fact that thicker skull can attenuate the energy more than a thinner skull, although the intensity difference through the skull would not be as large [24]. In addition, it has been studied that the radiation dose, resulting from CT imaging, is likely higher for the thicker skull patients [56].

To obtain an overall picture of the estimated skull thickness distribution along the selected patients, presenting the general neuro-HIFU patient population, a mean skull thickness of each patient was estimated. The original CT images were used to measure the true thickness in order to avoid any sizing or morphological alterations caused by the image registration. The mean skull thickness was estimated by first using the same bone mask extraction protocol as for the registered images, presented in Section 4.5. The thickness was calculated using the spherical linear model approach, presented in more detail in Section 4.6. A script for the thickness estimation was developed to calculate the skull thickness along each perpendicular line through the skull. The resulting minimum, maximum, and the mean thickness were saved to a file, together with the thickness range of each skull. The results are presented in Section 5.3.

The thicknesses were not calculated from the ZTE images as originally intended. Unfortunately, the true image size header information was systematically faulty for most of the ZTE images. Due to this, the true ZTE image size in world coordinates, and therefore, the skull size could not be replicated with certainty from the non-registered ZTE images. However, in theory, the skull thickness calculation from the ZTE images should be possible with good accuracy. Previous studies have shown that the thickness calculation is possible also from poorer quality ZTE images, with strong correlation ($r^2 = 0.97$, $p < 0.001$) compared to the CT-based thickness metrics [5]. Luckily, this header issue did not affect the SDR calculation, as due to the affine registration, the ZTE skull mask size was the same, as for the CT images. In addition, as the SDR calculation is intensity-based and not size-dependent metric, small errors in the size replication did not affect the SDR calculation.

4.8 Statistical analysis

A statistical analysis was performed to evaluate the relationship between the obtained SDR_{CT} and SDR_{ZTE} values, as well as their correspondence with the SDR_{true} , provided by the Insightec system. In addition, the relationship between the SDRs and the skull thickness values were evaluated. Key statistical metrics were calculated, including the means, standard deviations (SD), and variances of the SDRs from each modality and from the benchmark. In addition, mean absolute errors (MAE) and root mean squared errors (RMSE) were calculated for the comparisons between SDR_{CT} and SDR_{ZTE} values, SDR_{CT} and SDR_{true} values, and SDR_{ZTE} and SDR_{true} values.

To statistically evaluate the linear relationships between the datasets, Pearson correlation coefficients (r) and their corresponding p -values were calculated. The r measures the strength and direction of a linear relationship giving values between $[-1,1]$: values close to one indicate a strong positive correlation, values close to negative one indicate a strong negative correlation, and values near 0 suggest no linear correlation. For visualization, scatter plots with regression lines and 0.95 confidence intervals were generated.

To further evaluate the similarity and consistency not only for the SDR values but also in the intensity distributions of the CT and ZTE skull masks, a two-dimensional histogram analysis was performed to visualize the similarity between the log-scaled ZTE and CT image intensity distribution. In addition, as no single reliable method of comparing two such different modalities exists, visual inspection was used to compare the conventional CTs, unconventional CTs and their corresponding ZTE images. Direct statistical image comparison via e.g., subtraction was not sufficient, as the intensity values of single pixels are not comparable between the models. This means that the values in same pixels from different images are never the same between the modalities. The results of the analyses are presented in Chapter 5.

5 Results

This Chapter presents the findings from the research, which are then evaluated and interpreted in the Discussion Chapter 6. The metrics presenting the registration accuracy, explained in Section 4.3, are presented in Section 5.1. The obtained SDR values, calculated in Section 4.6, are presented in Section 5.2. The skull thickness values obtained in Section 4.7, are presented in Section 5.3. Most importantly, the correlation metrics calculated in Section 4.8, are presented in Section 5.4. The conclusions of this study are drawn based on this Chapter and the pipeline's performance in light of the data and previous studies.

5.1 Registration accuracy

The registration accuracy has an impact on how large area of the skull fits inside the ROI, which affects the intensity distribution from which the SDR was calculated. Therefore, accurate registration plays a role in the accuracy of the calculated SDR. The mean registration accuracy was significantly higher between the MR and ZTE images compared to the conventional CT and MR images as displayed in Table 5 below. The mean registration metric for the ZTE images was -0.63 , whereas for the CT images it was -0.39 .

Table 5: The achieved registration similarity metric values of CT and ZTE images for each patient, and their mean values for the two subgroups. The MMI algorithm is based on minimizing the negative mutual information value between two images. Therefore, a lower similarity metric value indicates greater mutual information and, consequently, better registration.

| Patient Nro. | Conventional CT Metric | ZTE Metric |
|--------------|------------------------|------------|
| 001 | -0.54 | -0.60 |
| 002 | -0.30 | -0.66 |
| 003 | -0.51 | -0.62 |
| 004 | -0.28 | -0.60 |
| 005 | -0.28 | -0.66 |
| 006 | -0.50 | -0.61 |
| 007 | -0.55 | -0.63 |
| 008 | -0.28 | -0.63 |
| 009 | -0.30 | -0.65 |
| 010 | -0.33 | -0.62 |
| 011 | -0.27 | -0.61 |
| 012 | -0.34 | -0.57 |
| 013 | -0.56 | -0.65 |
| 014 | -0.28 | -0.61 |
| 015 | -0.29 | -0.64 |
| 016 | -0.28 | -0.63 |
| 017 | -0.28 | -0.59 |
| 018 | -0.34 | -0.64 |
| 019 | -0.38 | -0.60 |
| 020 | -0.28 | -0.61 |
| 021 | -0.35 | -0.63 |
| 022 | -0.54 | -0.63 |
| 023 | -0.46 | -0.64 |
| 024 | -0.31 | -0.66 |
| 025 | -0.57 | -0.66 |
| 026 | -0.52 | -0.64 |
| 027 | -0.50 | -0.61 |
| 028 | -0.48 | -0.62 |
| 029 | -0.55 | -0.61 |
| Mean | -0.39 | -0.63 |

5.2 SDR values

The SDR values obtained from all modalities for each patient are presented in Table 6, along with the corresponding mean, standard deviation, and variance. These SDR values were calculated using Equation 2, which is explained in detail in Section 2.3.2,

and implemented in the algorithm described in Section 4.6.

Table 6: Table of all calculated SDR values, including SDR_{true} , conventional SDR_{CT} , and SDR_{ZTE} for each patient. Also the mean, standard deviation, and variance for each modality-derived SDRs are presented separately on the bottom of the table.

| Patient Nro. | SDR_{true} | SDR_{CT} | SDR_{ZTE} |
|---------------------|---------------------|-------------------|--------------------|
| 001 | 0.57 | 0.58 | 0.77 |
| 002 | 0.54 | 0.56 | 0.72 |
| 003 | 0.56 | 0.62 | 0.81 |
| 004 | 0.52 | 0.55 | 0.72 |
| 005 | 0.46 | 0.52 | 0.77 |
| 006 | 0.41 | 0.46 | 0.75 |
| 007 | 0.45 | 0.49 | 0.74 |
| 008 | 0.63 | 0.64 | 0.79 |
| 009 | 0.41 | 0.49 | 0.74 |
| 010 | 0.67 | 0.71 | 0.79 |
| 011 | 0.67 | 0.68 | 0.80 |
| 012 | 0.41 | 0.42 | 0.67 |
| 013 | 0.63 | 0.70 | 0.81 |
| 014 | 0.50 | 0.50 | 0.77 |
| 015 | 0.51 | 0.53 | 0.78 |
| 016 | 0.52 | 0.54 | 0.76 |
| 017 | 0.36 | 0.39 | 0.62 |
| 018 | 0.57 | 0.64 | 0.80 |
| 019 | 0.69 | 0.72 | 0.76 |
| 020 | 0.47 | 0.56 | 0.75 |
| 021 | 0.70 | 0.70 | 0.80 |
| 022 | 0.56 | 0.62 | 0.76 |
| 023 | 0.50 | 0.60 | 0.72 |
| 024 | 0.47 | 0.52 | 0.76 |
| 025 | 0.42 | 0.48 | 0.65 |
| 026 | 0.36 | 0.38 | 0.55 |
| 027 | 0.81 | 0.81 | 0.87 |
| 028 | 0.37 | 0.43 | 0.68 |
| 029 | 0.59 | 0.60 | 0.76 |
| Metric | | | |
| Mean | 0.5386 | 0.5671 | 0.7473 |
| SD | 0.1115 | 0.1045 | 0.0628 |
| Var | 0.0124 | 0.0109 | 0.0039 |

The acquired SDR values, calculated from the unconventional CT images, along with their corresponding SDR_{ZTE} and the SDR_{true} values, are presented in Table 7. Mean, standard deviation, and variance were not calculated due to the small sample size.

Table 7: SDR_{true} , SDR_{CT} from the unconventional CT images and SDR_{ZTE} for each patient.

| Patient Nro. | SDR_{true} | SDR_{CT} | SDR_{ZTE} |
|--------------|--------------|------------|-------------|
| 001_un | 0.47 | 0.49 | 0.74 |
| 002_un | 0.59 | 0.58 | 0.78 |
| 003_un | 0.64 | 0.60 | 0.77 |
| 004_un | 0.42 | 0.44 | 0.65 |
| 005_un | 0.36 | 0.38 | 0.58 |
| 006_un | 0.46 | 0.45 | 0.76 |

5.3 Skull thickness

The calculated skull thickness values, as described in Section 4.7 are displayed in Table 8 below. The Table includes the patient number, mean skull thickness, minimum and maximum thicknesses, and the range, all reported in millimeters. The bottom row displays the mean of all skull thickness means across all patients.

Table 8: The estimated skull thickness, and its minimum, maximum and the range for each patient.

| Patient Nro. | Mean (mm) | Min (mm) | Max (mm) | Range (mm) |
|---------------------|------------------|-----------------|-----------------|-------------------|
| 001 | 6.44 | 1.68 | 11.06 | 9.38 |
| 002 | 9.70 | 3.37 | 18.04 | 14.67 |
| 003 | 6.30 | 1.92 | 10.10 | 8.18 |
| 004 | 7.51 | 2.16 | 12.51 | 10.34 |
| 005 | 7.19 | 2.89 | 13.95 | 11.06 |
| 006 | 6.06 | 1.92 | 8.90 | 6.97 |
| 007 | 8.69 | 4.57 | 13.71 | 9.14 |
| 008 | 6.12 | 1.68 | 9.86 | 8.18 |
| 009 | 6.54 | 1.68 | 11.78 | 10.10 |
| 010 | 9.38 | 5.53 | 16.59 | 11.06 |
| 011 | 7.89 | 1.92 | 12.02 | 10.10 |
| 012 | 7.71 | 2.40 | 12.26 | 9.86 |
| 013 | 8.55 | 2.16 | 13.47 | 11.30 |
| 014 | 7.30 | 1.92 | 12.26 | 10.34 |
| 015 | 5.61 | 2.16 | 10.10 | 7.94 |
| 016 | 8.18 | 1.44 | 12.75 | 11.30 |
| 017 | 7.07 | 1.92 | 17.56 | 15.63 |
| 018 | 6.24 | 2.65 | 11.06 | 8.42 |
| 019 | 7.44 | 2.65 | 12.75 | 10.10 |
| 020 | 7.50 | 2.65 | 11.54 | 8.90 |
| 021 | 8.85 | 4.33 | 17.31 | 12.99 |
| 022 | 8.64 | 2.89 | 14.91 | 12.02 |
| 023 | 6.57 | 2.16 | 11.06 | 8.90 |
| 024 | 6.57 | 2.89 | 10.58 | 7.70 |
| 025 | 6.78 | 1.68 | 11.30 | 9.62 |
| 026 | 7.77 | 2.16 | 13.23 | 11.06 |
| 027 | 6.22 | 1.92 | 9.62 | 7.70 |
| 028 | 9.26 | 3.13 | 14.91 | 11.78 |
| 029 | 6.01 | 1.68 | 9.38 | 7.70 |
| Mean | 7.38 | | | |

5.4 Correlation

This Section combines the correlation metrics, calculated based on data presented in Sections 5.2 and 5.3. The Pearson correlation was calculated between all derived SDRs, as well as between the SDRs and the skull thicknesses. Additionally, visualization plots are included to illustrate the differences between the modalities in terms of the SDRs and their image intensity distributions.

5.4.1 SDR linear dependencies

The Pearson correlation coefficients, presented in Table 9 for the conventional set, were calculated between all three pairs: SDR_{true} and SDR_{CT} , SDR_{true} and SDR_{ZTE} , and SDR_{CT} and SDR_{ZTE} .

Table 9: The Pearson correlation coefficient between each modality-derived SDRs separately, and their corresponding p -values accordingly.

| | $SDR_{\text{true}} \& SDR_{\text{CT}}$ | $SDR_{\text{true}} \& SDR_{\text{ZTE}}$ | $SDR_{\text{CT}} \& SDR_{\text{ZTE}}$ |
|------------|--|---|---------------------------------------|
| r | 0.97 | 0.78 | 0.81 |
| p -value | < 0.0001 | < 0.0001 | < 0.0001 |

In order to assess the SDR error margins, the calculated mean absolute errors and root mean squared errors are presented in Table 10 below. MAE presents the average of the absolute differences between SDRs, while RMSE calculates the square root of the average of the squared differences. RMSE gives more weight to larger errors due to the squaring process, making it more sensitive to outliers than MAE.

Table 10: The mean absolute error and the root mean squared error between each modality derived SDRs separately.

| | $SDR_{\text{true}} \& SDR_{\text{CT}}$ | $SDR_{\text{true}} \& SDR_{\text{ZTE}}$ | $SDR_{\text{CT}} \& SDR_{\text{ZTE}}$ |
|-------------|--|---|---------------------------------------|
| MAE | 0.0387 | 0.2187 | 0.1802 |
| RMSE | 0.0022 | 0.0533 | 0.0367 |

The achieved correlation between the SDR_{true} and the conventional SDR_{CT} is highest among the three groups, 0.97, as displayed in Table 9 and the Figure 16 below. The unconventional SDR_{CT} values are also displayed in the Figure, together with the 0.95 confidence intervals for both sets. A linear regression fit has been applied to the data points, and the Figure's legend displays the slopes, Pearson correlation coefficients and the p -values accordingly. The dashed line presents the $x = y$ line, where all SDR values would be the equal between the modalities. The validation of the model was performed based on this linear relationship.

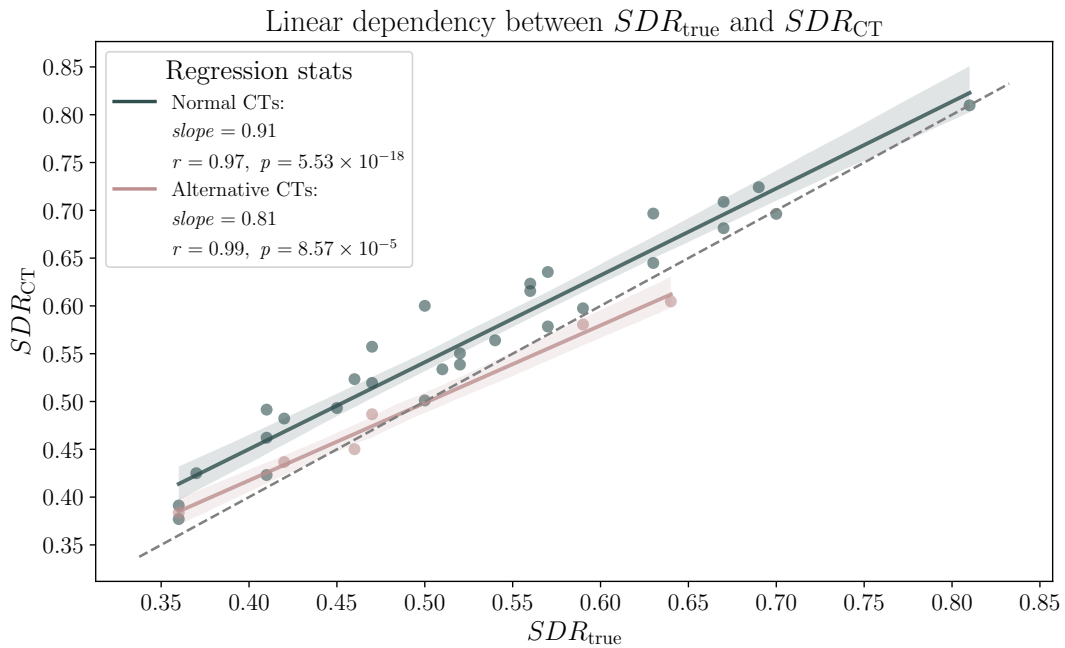
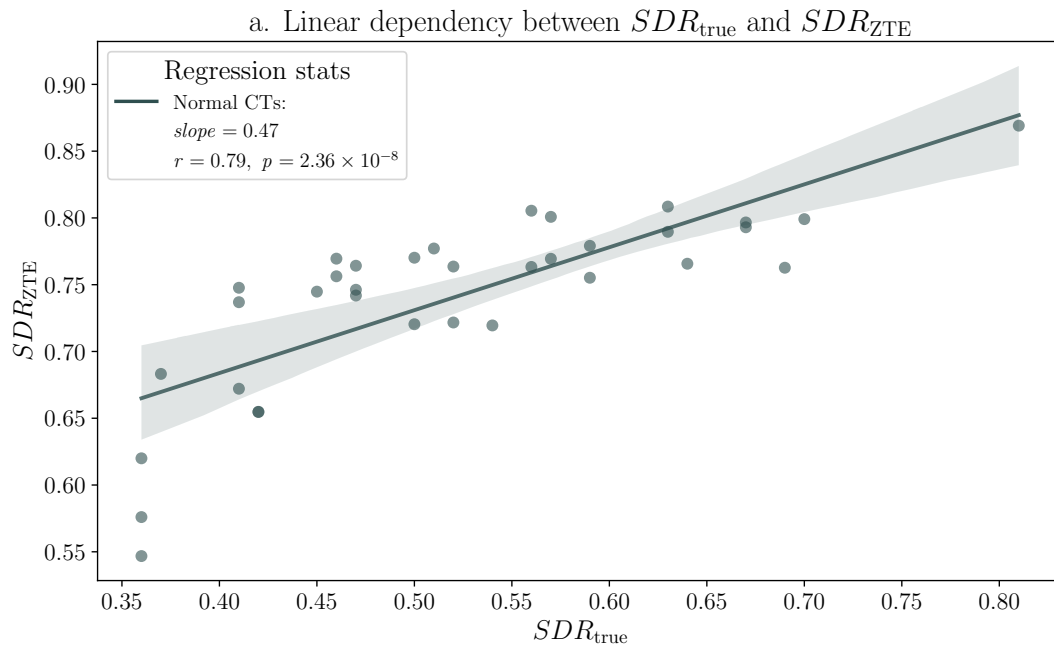
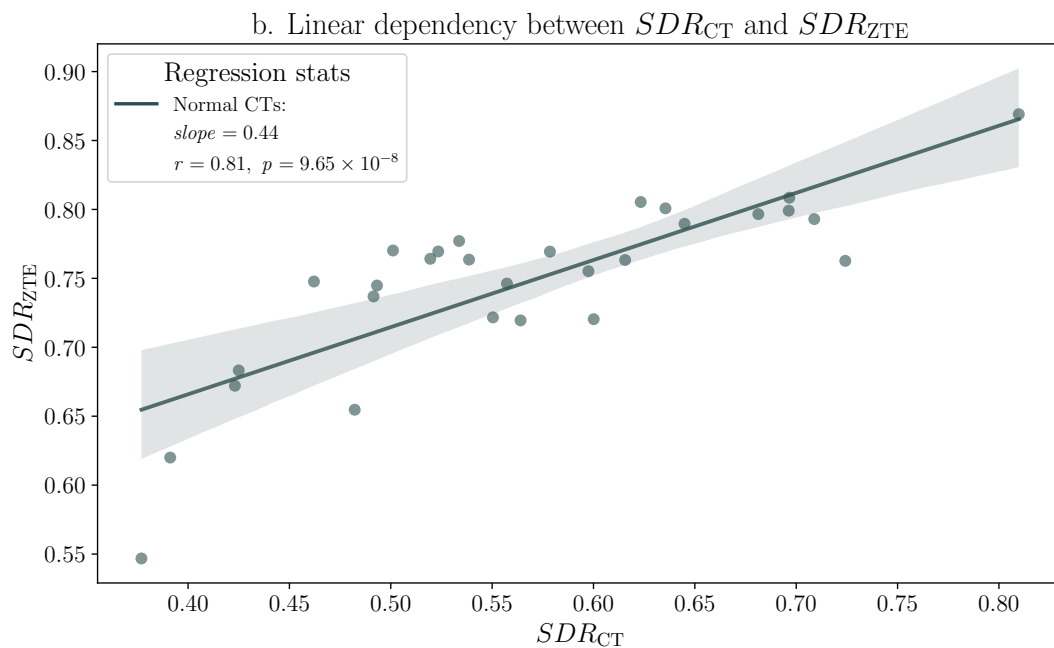


Figure 16: A regression plot with 0.95 confidence intervals showing the linear dependency between the obtained SDR_{true} and the SDR_{CT} values. The Pearson correlation coefficients (r), p -values and slopes are included in the legend.

The linear dependency between the obtained SDR_{true} and SDR_{ZTE} , as well as between the SDR_{CT} and SDR_{ZTE} are visualized in Figures 17a and 17b below. A linear regression fit that minimizes the sum of squared residuals between the data points and the line has been applied to the datasets. Furthermore, the legends display the slopes, Pearson correlation coefficients, and the p -values accordingly. The achieved high positive r between SDR_{true} and SDR_{ZTE} was 0.79, and 0.81 for the SDR_{CT} and SDR_{ZTE} pair. Both p -values were well below 0.0001, and all CT-based SDRs were obtained from the conventional CT dataset.



(a) A regression plot with confidence interval showing the linear dependency between the SDR_{true} and the SDR_{ZTE} values. The dataset included all 35 patients.



(b) A regression plot with confidence interval showing the linear dependency between the SDR_{CT} and SDR_{ZTE} values.

Figure 17: Linear regression plots for the linear dependencies between (a) the SDR_{true} and the SDR_{ZTE} , and between (b) SDR_{CT} and SDR_{ZTE} . Legends are displaying the key metrics, and the light area represent the 0.95 confidence intervals.

5.4.2 Accuracy margin

The differences in the error margins of the SDR_{CT} and SDR_{ZTE} values, when both groups are compared against the benchmark SDR_{true} values, are also shown in binned confusion matrix Figures 18 and 19 below. The Figures show how close the calculated SDR is to the corresponding SDR_{true} , and with what margin. The bin widths in the Figures are 0.05. Figure 18 below displays the difference margin of SDR_{CT} values to the corresponding SDR_{true} values.

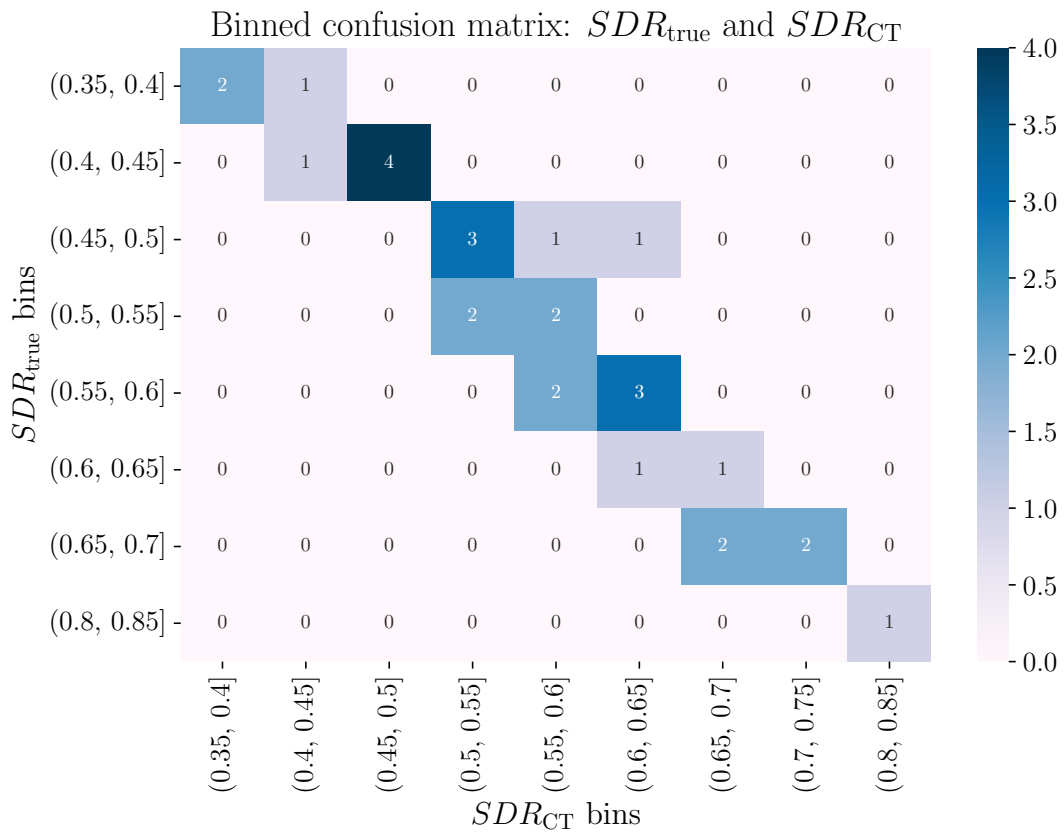


Figure 18: Binned confusion matrix for the SDR_{true} and the corresponding conventional SDR_{CT} values. Bin sizes are displayed in the x and y axis.

Furthermore, the similar binned confusion matrix between the SDR_{ZTE} and SDR_{true} values is shown in Figure 19 below.

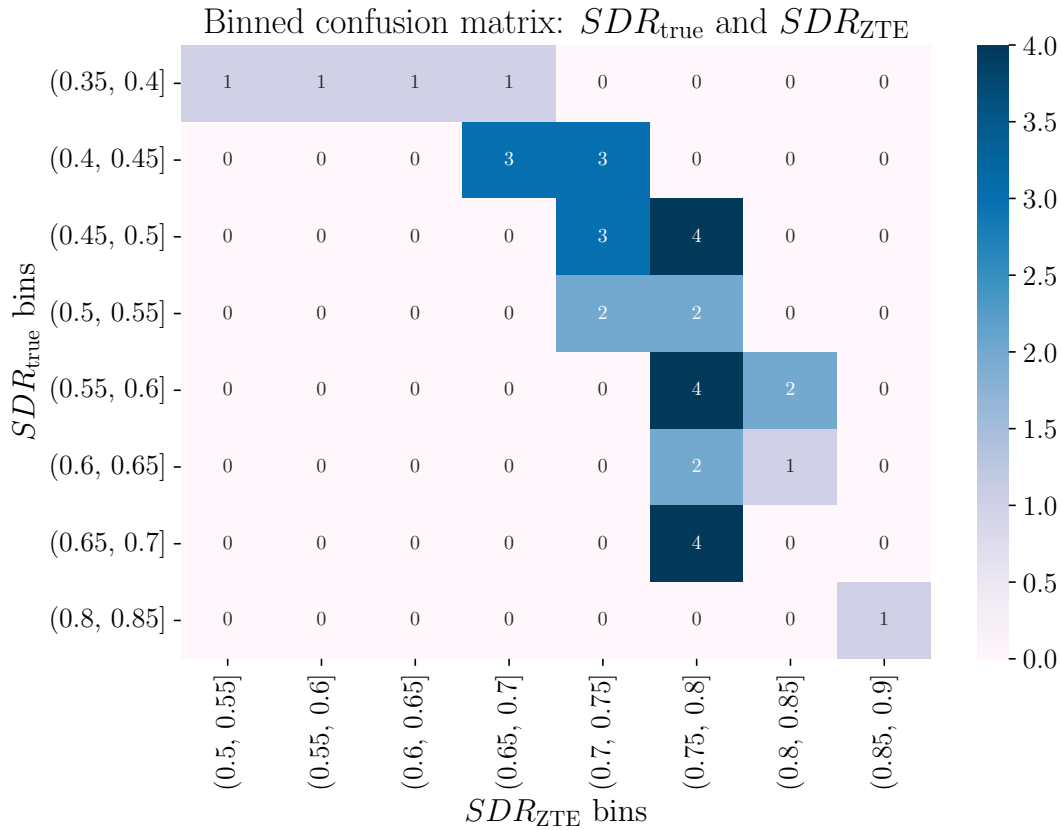


Figure 19: Binned confusion matrix for the SDR_{true} values and all 35 SDR_{ZTE} values. The bin sizes are again displayed in the x and y axis.

5.4.3 Intensity similarity

In addition to the SDR correlation and linear dependency between the values, a two-dimensional histogram distribution was derived from one CT and ZTE skull volume pair, to visualize the similarity between the high and low HU and intensity areas between the images. Figure 20 presents the 2D histogram of a patient's CT and ZTE skull caps. The dark red area in the Figure corresponds to the HU and intensity values of the corresponding cortical bone areas.

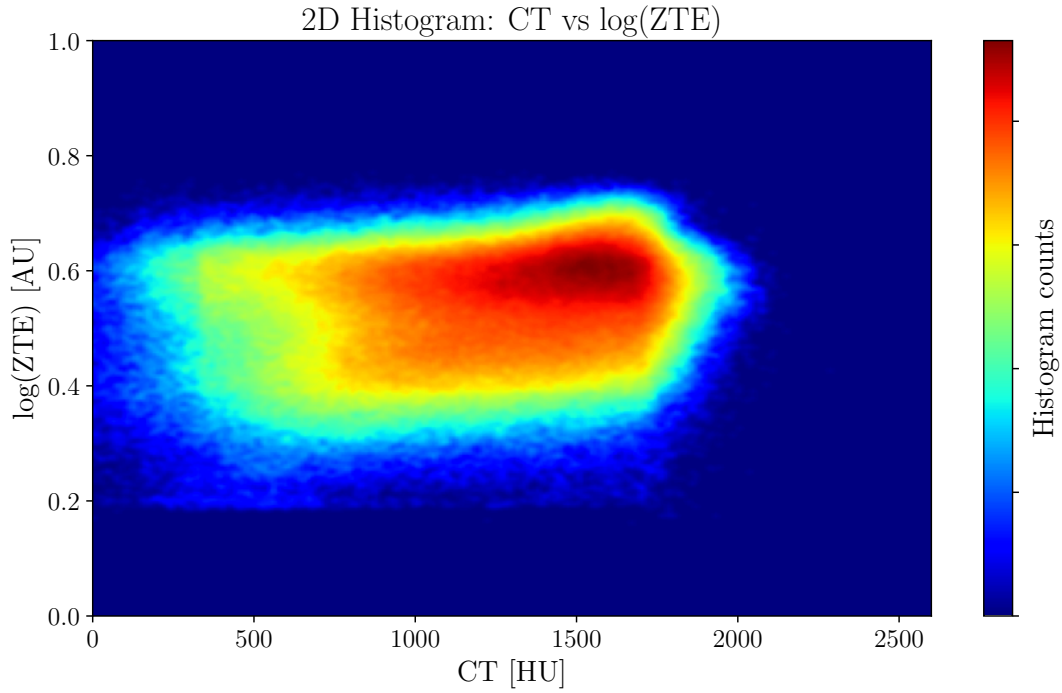


Figure 20: Example of a 2D histogram comparing the intensities of the CT and log-transformed ZTE skull cap volumes. The red region highlights areas of mutual high intensity in corresponding locations of both images. The color bar indicates the histogram counts.

5.4.4 Skull thickness and SDR

Lastly, the correlation between the calculated skull thicknesses and all corresponding SDRs were calculated. The thickness estimates were reported in Section 5.3 and the corresponding SDRs in Section 5.2. The obtained Pearson correlation metrics are presented in Table 11 below.

Table 11: The Pearson correlation coefficient between the derived skull thickness and the derived SDR values, in addition to the corresponding p -values.

| | $SDR_{\text{true}} \& \text{Thick.}$ | $SDR_{\text{CT}} \& \text{Thick.}$ | $SDR_{\text{ZTE}} \& \text{Thick.}$ |
|------------|--------------------------------------|------------------------------------|-------------------------------------|
| r | 0.032 | 0.017 | -0.14 |
| p -value | 0.87 | 0.93 | 0.46 |

6 Discussion

This Chapter analyzes, interprets, and concludes the findings presented in Chapter 5. The interpretation of the results is done throughout Section 6.1 in relation to the research questions introduced in Chapter 1. The limitations of the study are discussed in Section 6.2. The significance of the findings and practical implications are outlined in Section 6.3. Lastly, suggestions for further research in the field are discussed in Section 6.4.

The primary objective of this Master’s Thesis was to investigate the suitability of using ZTE MRI as a clinically viable alternative for CT imaging in the context of HIFU treatment planning. To our knowledge, this was the first time taking an intensity profile-based approach to study the comparability of ZTE and CT-based SDRs. This was done by creating a semi-automatic pipeline, based on the existing mathematical equations, to calculate the needed skull measures from both modalities. A correlation analysis was performed between the datasets and against the benchmark values to assess, whether skull attenuation characteristics can be calculated in statistically significant detail from ZTE images. In addition, the image quality and clinical utility of ZTE was compared to the conventional CT scans in the context of HIFU planning. Using the data introduced in Chapter 3 and based on the analysis explained through Chapter 4, the results presented in Chapter 5 suggest that ZTE images can pose an alternative option for CT images in neuro-HIFU treatment planning. Therefore, if sufficient preprocessing methods, presented in Section 4.2, are applied, the GE SIGNA Premier 3T ZTE MRI can provide sufficient anatomical detail without the need for supplementary CT imaging.

6.1 Pipeline performance

To assess the reliability of the obtained results, the pipeline was first validated with the conventional CT images. High correlation ($r = 0.97$, $p < 0.0001$) with the benchmark SDRs was achieved, as displayed in Table 9 and the Figure 16. This implies that the developed image registration and SDR calculation pipeline provided expected and sufficient results, comparable to the Insightec modality. In addition, this was proven by the unconventional SDR_{CT} values that are also displayed in the Figure 16, together with the 0.95 confidence intervals. This suggests that the pipeline was accurate, and therefore, reliable in calculating the needed measures. Based on these validation results, it was concluded that the ZTE-based SDRs would be derivable with the developed pipeline.

During the registration steps of the pipeline, the mutual information metrics were saved, and the registration accuracy was visually confirmed. The lower registration mutual information metric of the CT images, presented in Table 5, does not directly mean that the registration would be significantly inferior compared to the ZTE registrations with the same anatomical MRIs, but that the mutual information between the images is different due to the different image characteristics. The higher mutual information between the MR and ZTE images can be explained by the similar intensity values, the ZTE showing more anatomical landmarks compared to the CT images,

and by the similar original positioning of the images, as the MR and ZTE images were acquired in the same session. However, it was confirmed during the analysis that the registration accuracy was higher between the MRI and ZTE images, than between the MRI and CT images. Therefore, it is expected that implementing the ZTE SDR calculation modality into the Insightec system might obtain better results elsewhere, as the registration between the pretreatment images is likely stronger.

6.1.1 SDR comparability

As explained through Chapter 5, shown in Table 9, and regression Figures 16, 17a, and 17b, all calculated SDR value groups exhibit very high positive and statistically significant correlation. All p -values indicated that the results were statistically significant, suggesting that the null hypothesis is unlikely to be true.

Based on the high statistical correlation metrics ($r = 0.78$, $p < 0.0001$) calculated for the SDR_{true} and the SDR_{ZTE} presented in Chapter 5, zero echo time magnetic resonance imaging would pose a potential alternative for CT-based SDR values in neuro-HIFU treatment planning. In addition, the correlation between the SDR_{CT} and SDR_{ZTE} values was stronger than the SDR_{ZTE} against the benchmark SDR_{true} values, implying that the error in the pipeline is skewed in the same direction for both modalities. However, it can be noted how the confidence interval is significantly narrower in the SDR_{CT} plot, 16, compared to the SDR_{ZTE} plot 17a. In addition to that the obtained SDR_{ZTE} values were significantly higher, with difference in means being 0.18, when compared to the SDR_{true} values. These results imply that the uncertainty in accuracy of SDR_{ZTE} values is larger, when compared against the CT-based values.

Therefore, it must be considered that the standard deviation of 0.0628 and variance of 0.0039 of the SDR_{ZTE} is smaller, when compared to the true deviation of 0.1115 and variance of 0.0124 of the SDR_{true} values, as presented in Table 6. This implies that the range of SDR_{ZTE} values is narrower and thus, small differences in the SDR are more distinguishable from CT images than from ZTE images, when using the methods presented in this study. The same conclusion can be drawn based on the MAE and RMSE errors presented in Table 10. The SDR_{ZTE} group had the largest errors, MAE of 0.2187 and RMSE of 0.0533, when compared to the the SDR_{true} value distribution. These errors were significantly more, compared to the SDR_{CT} -derived MAE of 0.0387 and RMSE of 0.0387.

This same reduced accuracy and larger error can be seen from the binned confusion matrices in Figures 18 and 19. Although not all of the calculated SDR_{CT} values fall into the true bins with 0.05 accuracy in Figure 18, majority of the calculated values are within 0.1 margin form the SDR_{true} value. Whereas none of the SDR_{ZTE} values fall into the correct bins, as presented in Figure 19. It can also be seen from the binned confusion matrices that the uncertainty of SDR_{ZTE} values does not follow the same linear manner as for the SDR_{CT} values. This implies that the error in between SDR_{ZTE} values is not skewed in the same direction, thus bringing uncertainty. The smaller deviation but larger error of the SDR_{ZTE} values tell that an individual SDR value might not be as distinguishable from other SDR, and thus, they are more packed along the range, compared to the distribution of the SDR_{true} values. This can also be concluded

from the reduced slopes in Figures 17a and 17b, when compared to the slope of Figure 16. These observations do not solely imply that the SDR_{ZTE} values would not be sufficient to estimate the skull attenuation properties. However, it is evident that the SDR calculation from ZTE images is not as robust as from the CT images. However, this was expected due to the lower contrast properties of ZTE images.

Therefore, some additional details must be taken into account when planning to implement SDR_{ZTE} as a skull attenuation estimation measure into clinical use. If ZTE is validated as a pretreatment skull value calculation modality for HIFU treatment planning, the conventionally used SDR inclusion limit of 0.3–0.35, used in EU, is unsuitable. This is because it was confirmed that ZTE images produce higher SDR values due to the naturally different contrast properties of the images. Therefore, patient's SDR_{ZTE} is different when compared to the SDR_{CT} value due to the superb contrast of CT images. As the 0.3–0.35 EU limit and 0.45 FDA limits are specifically used as a threshold for SDR calculation from CT images, a novel limit must be introduced for the ZTE-based values. Low limit would most likely include patients with false positive suitability for HIFU, as low SDR_{true} values imply relatively high SDR_{ZTE} values as presented in Figure 17a. Based on this study, the used material, and results in Figure 17a, the linear dependency between SDR_{true} and SDR_{ZTE} can be derived as

$$SDR_{ZTE} = 0.471 \cdot SDR_{true} + 0.495, \quad (5)$$

where SDR_{ZTE} indicates ZTE-based SDRs and SDR_{true} is the true, benchmark SDRs. Therefore, by implementing the TYKS SDR inclusion threshold of 0.35 to Equation 5, we get 0.66 as the SDR_{ZTE} -based inclusion threshold.

When we calculate the dependency for the SDR_{ZTE} and the SDR_{CT} values acquired in this study via the same method, based on results presented in 17b, we get

$$SDR_{ZTE} = 0.439 \cdot SDR_{CT} + 0.515, \quad (6)$$

where SDR_{ZTE} indicates ZTE-based SDR and SDR_{CT} is the CT-based SDR. And again, by implementing the SDR inclusion threshold of 0.35 to Equation 6, we get 0.67 as the SDR_{ZTE} -based inclusion threshold. Thus, SDR_{ZTE} around 0.66–0.67 could be suggested to be the subject of further ZTE-based inclusion criteria research.

Overall, the acquired SDR_{ZTE} values followed the theory-based predictions introduced in Section 2.5. The SDR_{ZTE} values were expected to be higher, due to the naturally lower contrast in ZTE images. The calculated correlation between the SDR_{ZTE} and SDR_{true} values was comparable to the predictions made in previous studies. Therefore, it can be concluded that the SDR can be estimated from the ZTE images, although, the accuracy and robustness of the prediction is slightly reduced.

6.1.2 Thickness estimation

As mentioned in Section 4.7, the skull thicknesses were only calculated from the original conventional CT images, and not from the original ZTE images as intended. Unfortunately, the true ZTE image size header information was systematically faulty for most of the ZTE images, thus consequently, the true size of the ZTE image in

world coordinates could not be replicated accurately. It remained uncertain whether the header issue resulted from the image acquisition parameters or from the used platforms' inability to interpret the headers. Although unlikely, it can be possible that the platforms' were unable to detect the needed parameters in the header of such novel image format. Only preliminary results can be estimated from the registered images, whose true sizes are likely affected by the affine transformations from the registration. Therefore, the thicknesses were only calculated and reported from the original CT images.

The calculated skull thickness values in Table 8 seem to present the normal range of adult Caucasian skull thicknesses, with the average (7.38 mm) being on the higher end of the normal range, when compared to the values calculated by Moreira and colleagues [57]. However, this was expected, as few patients in the dataset had benign overgrowth of the skull, making the thickness significantly higher than of normal adult. The average skull thickness of these patients was closer to 9 mm. Some patients had overgrowth only on the frontal bone, and some patients had a thicker skull across the whole volume. As can be seen from Table 11, the correlation is indecisive, which was expected, as previous studies have not found correlation between the patient's skull thickness and the SDR.

Although the thicknesses of the ZTE images could not be calculated in statistically significant detail, some preliminary runs were performed for the registered image pairs. Based on the semi-empirical preliminary results, it can be suggested that the thicknesses were close to similar between the CT and ZTE images, but the ZTE thicknesses were slightly overestimated. Empirically, this is most likely due to the fact that the segmentation is not as accurate as for the CT images due to the reduced boundary accuracy. This aligns with the findings of previous research done to the topic. However, these runs were done solely out of interest and do not obtain any statistically significant information. Thus no conclusions can be made but the possibility of calculating the thickness from ZTE images cannot be excluded. Per previous studies, the calculation from ZTE image should have been possible, with similar detail than for the CT images.

6.1.3 Visual evaluation

Measuring the micro-scale morphological differences between the conventional, unconventional and ZTE images is not possible in statistically significant detail due to the resolutions of all images being too low, compared to the sub millimeter scale of some skull structures. Therefore, this Section only makes notes regarding the visual aspect and thus, the empirical image quality of the three different modalities. After going through 70 images multiple times — out of which 35 were ZTE, 29 from conventional CT, and six from older generation, unconventional CT scanner — the differences in image quality became evident.

It was noticed during the analysis, that the detail in the conventional CT images was considerably the highest within the group. The differences were not as noticeable when looking at the whole image volumes, compared to the differences in fine details which were more visible in the smaller volume skull caps. This can be seen from

example in Figures 10, 11, and 12, although not all three images are from the same patient. In addition, the broader skull intensity distribution can be seen in Figure 20. The histogram bin amount is the same in both axis of the Figure, but the distribution is more extensive in the CT images, allowing better image contrast. It was confirmed that this feature was not dependent on visualization properties.

The higher detail and contrast of the conventional CT images helped in the segmentation steps, as the difference between the cortical bone and other tissues were sharp. Interestingly, it was noticed that segmenting the unconventional CT and the ZTE was, objectively, very similar. In most cases the ZTE seemed to even replicate the true landmarks, such as the sutures, more distinguishable compared to the unconventional CTs. The sutures were most accurately replicated in the conventional CTs but were also very notifiable in the corresponding ZTE images.

The differences between the image qualities are not only due to the FOV, matrix size and thus, pixel size of the images, but also how the modality replicates the contrast and detail. In addition, the noise present in the images plays a huge role in the resulting signal to noise and contrast to noise -ratios. Given this, it was evident that the ZTE images and the unconventional CT images were surprisingly close to each other, in terms of clinical detail and quality, and the detail in the conventional CT was superior compared to them. However, it was also apparent, how the unconventional CT replicated the contrast between the trabecular and cortical bone significantly better, than the ZTE images.

Although it was proven that the ZTE image resolution was lower, and the contrast did not reach that of a conventional CT image, it was confirmed that skull attenuation estimated, such as the SDR, can be calculated in statistically significant detail from the ZTE images.

6.2 Limitations of the study

Although, ZTE-based SDR calculation has not been widely studied, it can be concluded that this study is repeatable. This is because the methods used have their basis in existing equations and methods, combined from across multiple other studies. All obtained results were in concordance with the results and predictions made in previous studies.

However, sources of error might result from image resampling during the registration, and from the used interpolation during it. When an image is transformed to the space of another image, resampling and interpolation is needed in the transformation. As the analysis was extremely intensity-sensitive, the SDR algorithm had slightly better performance with the original, unprocessed images, compared to the registered images. The impact of interpolation and resampling on image quality and intensity distribution was minimized by selecting the most suitable interpolator based on theory and empirical evidence. As changes in the intensity distribution directly impact the calculated SDR, all preprocessing and filtering was kept as minimal as justified throughout the analysis.

In addition, manually thresholding the skull bone mask in 3D Slicer might be a source of error. Although the intensity histogram values were taken into account

while segmenting the calvaria, it is likely that the thresholds were not exactly on the boundary values of the bone in all slices of the image, due to the partial volume effect, interpolation in the resampling, and possible inhomogeneities in the imaging modalities. While segmenting the bone masks, the threshold was selected so that the resulting mask truly included all bone voxels, and no bone was masked out. As some partial volume voxels were likely included in the final bone masks, the SDR and the thickness algorithms disregarded these values. This was noticed to be important aspect to include into the algorithms, as in areas with only cranial bone, the minimum intensity calculated might have resulted from the partial volume effect and not from the true bone. After validating this fallback logic to the algorithms, their performance was greatly increased.

It should be noted, the SDR algorithm does not model the true HIFU beam path accurately, as the linear line through the skull does not get refracted nor reflected in the boundaries. However, the impact of the non-linear true beam path on the calculated SDR would probably be negligible as high amount of linear paths cover the skull surface evenly. As the skull volume is sampled with a great number, and the distance between the correctly refracted beam path and the modeled linear beam paths is minor, the difference between the paths is likely averaged out over the vast amount of samples. However, if the interest would be in the localization of the focal point, the accurate modeling of the true beam path would be crucial.

It must also be noted that the skull thickness calculation presented in Section 4.7, and its results displayed in Section 5.3 are an estimation as long as the patient is alive. I estimate that the thickness is calculated with high accuracy, but the partial volume effect on the skull boundaries and near thin regions may overestimate the thickness. The true skull thickness can only be calculated by measuring the physically stripped skull of the patient.

Other sources of error might include the ROI selection, as it is known that the skull area left under the true HIFU treatment helmet usually follows the AC–PC plane, which is slightly below the plane chosen in this study. Thus, the true area under the helmet is slightly larger, than the skull area used in this study.

The obtained SDR_{ZTE} values were higher than SDR_{true} values. This difference can be justified by the poorer contrast in ZTE images. This contradicts with the study performed by Caballero and colleagues, who obtained ZTE-based SDR values that were smaller than the true values [5]. However, their study methods were fully based on the morphology and intensity-based segmentation of the trabecular and the cortical bone, which has been proven to be unsuitable as discussed in Section 2.4.2.

In addition, Wiesinger and colleges have stated that the intensity correlation between log-scaled ZTE images and normal CT images is approximately linear [10]. However, they studied low-dose CT HU values between 300 HU and 1500 HU, which are corresponding to soft-tissue and bone. As the CT used in this study was not low-dose, and the studied HU range was different, no direct conclusions can be made about the linearity based on the study of Wiesinger.

6.3 Significance and practical implications

The developed pipeline and the research results present several valuable implications for both research and clinical practice. The pipeline's efficiency, accuracy, and ability to run locally make it a practical tool for researchers and clinicians for potential further use. The scripts will be publicly available on GitHub, if the needed permissions are acquired, allowing others in the field to use, modify, and further develop the algorithm, which can significantly reduce the time and resources needed for similar studies. Its implementation in Python additionally enables easy integration of additional fallback logic and enhancements.

From a research perspective, the pipeline can be used as a foundation for future studies and clinical validation efforts, particularly in confirming ZTEs accuracy and robustness. Notably, ZTE shows resilience in the presence of metal artifacts, which are common in elderly patients with implants or amalgam fillings. This suggests ZTEs promising utility even in more complex clinical cases.

The advantages of the usage of ZTE in HIFU pretreatment phase include the possibility of streamlining the pretreatment process as ZTE images can be acquired simultaneously with the anatomical MR images. From a cost and radiation protection perspectives this would be a positive improvement. From a data preprocessing perspective, utilizing ZTE acquired simultaneously with the conventional MR images would likely bring better registration accuracy, which might imply higher quality treatment results in some cases. However, it also seems that there is no established intensity distributions or standard ZTE sequences that would be able to produce ZTE images with uniform quality and intensity distribution from patient to another. This is seen in the varying intensity distributions and voxel sizes across the ZTE dataset. This itself does not affect the quality of the images itself, but increases the need of image preprocessing.

The most prominent disadvantage in using ZTE-based measures in HIFU treatment planning is the naturally poorer resolution of ZTE images compared to conventional CT images. Although the GE SIGNA Premier 3T can produce superior ZTE images, they do not quite meet the quality of top-grade CT images in terms of resolution and contrast. The naturally lower contrast in the ZTE images induces uncertainty to the segmentation procedures in boundaries and fine bone structures. This is because the skull itself is not as distinguishable from the background compared to that of high-quality CT, and the lower resolution gives a raise to the increased tissue interface effects, decreasing the image precision on tissue boundaries. Due to this, it seems that the skull segmentation from ZTE might be overestimated, compared to that done to top-grade CT images with sharper boundary areas. However, when comparing the ZTE images to a older generation CT images, the differences are not as noticeable.

Overall, the results indicate a potential to reduce reliance on radiation-based imaging during the treatment planning process. Specifically, the ability to generate reliable skull images may help decrease the need for additional CT imaging, especially when ZTE sequences can be acquired alongside the standard anatomical MRI. This could streamline pretreatment workflows by reducing the number of imaging appointments, freeing up CT scanner availability, and lowering patient exposure to ionizing radiation.

This is particularly beneficial for elderly or vulnerable patients, as it shortens and simplifies the preparation process, reducing stress and logistical complexity during the treatment planning. Therefore, the pipeline and its results contribute directly to improving neuro-HIFU treatment planning and lay the groundwork for further research, development, and clinical integration of MRI-only workflows.

6.4 Suggestions for further research

Further research in the potential use of ZTE MRI as a replacement for CT in HIFU treatment planning will require close collaboration with Insightec. Transitioning from CT to ZTE imaging in SDR calculation requires rigorous validation of ZTE, and its inclusion criteria SDR threshold. The research would also need to include qualitative analyses of ZTEs SNR and contrast to noise ratios, as well as overall compatibility with Insightec's systems and algorithms. In addition, as the CT images are not only used for the SDR calculation, but also for phase correcting the beams, and visualizing the brain calcification, the validation would need to also include those. Luckily, previous research has given promising results regarding using ZTE in phase correction as well [52]. However, a short discussion with Insightec representatives indicated interest in such collaboration [34].

As the number of HIFU treatments continues to grow, streamlining the imaging pipeline by introducing ZTE could offer significant clinical and operational benefits, although the accuracy might not be the same as for CT images. Specific areas of investigation include ZTEs robustness to imaging artifacts and its performance in patients with low SDR, which is particularly important since CT radiation doses tend to increase as SDR decreases. This is because when the head and skull size increase, the required dose increases [56]. Consequentially, a low SDR and thicker skull can indicate a larger CT dose required to achieve the needed image quality [56, 24]. Therefore, ZTE could provide meaningful advantages especially for patients with low SDR and thicker skull, and to the clinical teams treating them.

Currently, one of the major limiting aspects for ZTE image quality is in the speed of capturing the FID signal. Therefore, studying the possibility of making the current hardware, especially coils, even more efficient would have direct impact on the ZTE image quality and contrast.

A broader study focusing on Finnish patient populations would also be valuable, given the high prevalence of hereditary conditions in Finland that affect skull morphology, size, and density which are factors directly influencing the SDR. Additionally, the high national prevalence of Parkinson's disease and essential tremor underscores the importance of improving and personalizing HIFU treatment planning for various patient subgroups. Exploratory work such as bone morphology assessment using micro-CT and general SDR profiling in Finnish cohorts could further support this aim. In addition, evaluating the compatibility of various CT machines could identify whether the SDR is a machine specific measure more than an individual based measure would help understanding SDRs importance and robustness as a skull characteristics estimation technique.

7 Conclusions

The objective of this Thesis was to investigate the feasibility of zero echo time magnetic resonance imaging in neuro-HIFU pretreatment planning. The ZTE images of 35 essential and Parkinson's tremor patients were studied by comparing them to the conventionally used CT images. This was done by calculating the same pretreatment measures from both image sets, and then by comparing the acquired measures. For this purpose, a semi-automatic analysis pipeline was created. The pipeline first prepossesses and coregisters the ZTE and CT images with the patient's anatomical T1-weighted MR image. After image postprocessing, skull calvaria masks are created from both image sets, after which they are used to calculate the skull density ratio, the key success measure for neuro-HIFU planning. The SDR and other measures are then analyzed and compared between the modalities by the pipeline.

Based on the analysis performed, it is suggested that ZTE poses a potential alternative for CT-based measures in neuro-HIFU treatment planning. This is due to its ability to produce adequate images from low proton density structures such as the skull. It was confirmed that ZTE images can reproduce the needed intensity-based measures with sufficient accuracy, compared to those obtained via CT scans.

The pipeline achieved high accuracy in SDR calculation, when tested with the conventional CT images ($r = 0.97$, $p < 0.0001$), meaning that the classified SDR algorithm was recreated accurately in this Thesis. Achieved correlation between the true, benchmark SDR values and the ZTE-derived SDR values was also significant and positive ($r = 0.78$, $p < 0.0001$). No correlation was found between the skull thicknesses and their SDRs. All results acquired in this Thesis were in accordance with previous research, done with lower quality ZTE images and smaller datasets. To our knowledge, this Thesis was the first study taking an intensity-profile based approach when comparing ZTE and CT-based skull attenuation estimates, therefore confirming the feasibility of ZTE in neuro-HIFU treatment planning.

The advantages of ZTE imaging include silent scanning, robustness against artifacts, and better registration accuracy with anatomical MR images. Although the ZTE images were able to reproduce the needed measures with anatomical detail, it was demonstrated that the produced ZTE images fall behind in image quality and accuracy in fine structures, and slightly in contrast, when compared to top-grade CT images.

Suggestions for future research include ZTE validation for neuro-HIFU pretreatment planning. In addition, the suggested SDR_{ZTE} inclusion criteria threshold requires further research. However, such validation would require close cooperation with Insightec, as well as ZTE validation not only for SDR and skull thickness calculation, but also for phase correction during the treatment. In addition, the research and development of the high-performance transmit/receive RF MR coils would greatly improve the quality of the ZTE images, as capturing the FID signal even earlier would most likely produce better contrast. Excluding the CT imaging from neuro-HIFU treatment protocol would help to streamline the pretreatment process, possibly reduce the costs, and most importantly, reduce the radiation dose received by the tremor patients.

References

- [1] A. Brück, R. Blanco Sequeiros, J. Frantzén, O. Hartiala, J. Hirvonen, P. Jokinen, J. Joutsa, S. Jääskeläinen, J. Korpela, T. Kuusimäki, et al. Kohdennettu ultraääni vapinan hoidossa. *Duodecim*, 2023.
- [2] S. Moosa, R. Martínez-Fernández, W. J. Elias, M. Del Alamo, H. M. Eisenberg, and P. S. Fishman. The role of high-intensity focused ultrasound as a symptomatic treatment for parkinson’s disease. *Movement Disorders*, 34(9):1243–1251, 2019.
- [3] G. ter Haar and C. Coussios. High intensity focused ultrasound: physical principles and devices. *International journal of hyperthermia*, 23(2):89–104, 2007.
- [4] Z. Izadifar, Z. Izadifar, D. Chapman, and P. Babyn. An introduction to high intensity focused ultrasound: systematic review on principles, devices, and clinical applications. *Journal of clinical medicine*, 9(2):460, 2020.
- [5] J. Caballero-Insaurriaga, R. Rodríguez-Rojas, R. Martínez-Fernández, M. Del-Alamo, L. Díaz-Jiménez, M. Ávila, M. Martínez-Rodrigo, P. García-Polo, and J. A. Pineda-Pardo. Zero te mri applications to transcranial mr-guided focused ultrasound: patient screening and treatment efficiency estimation. *Journal of Magnetic Resonance Imaging*, 50(5):1583–1592, 2019.
- [6] G. P. L. Thomas, T. D. Khokhlova, O. A. Sapozhnikov, Y.-N. Wang, S. I. Totten, and V. A. Khokhlova. In vivo aberration correction for transcutaneous hifu therapy using a multielement array. *IEEE transactions on ultrasonics, ferroelectrics, and frequency control*, 69(10):2955–2964, 2022.
- [7] A. Vetkas, A. Boutet, C. Sarica, J. Germann, D. Gwun, K. Yamamoto, H. H. Jung, A. Alkhotani, N. Samuel, S. Lang, et al. Successful magnetic resonance–guided focused ultrasound treatment of tremor in patients with a skull density ratio of 0.4 or less. *Journal of Neurosurgery*, 140(3):639–647, 2023.
- [8] K. W.-K. Tsai, J.-C. Chen, H.-C. Lai, W.-C. Chang, T. Taira, J. W. Chang, and C.-Y. Wei. The distribution of skull score and skull density ratio in tremor patients for mr-guided focused ultrasound thalamotomy. *Frontiers in Neuroscience*, 15:612940, 2021.
- [9] S. B. Cho, H. J. Baek, K. H. Ryu, B. H. Choi, J. I. Moon, T. B. Kim, S. K. Kim, H. Park, and M. J. Hwang. Clinical feasibility of zero te skull mri in patients with head trauma in comparison with ct: a single-center study. *American Journal of Neuroradiology*, 40(1):109–115, 2019.
- [10] F. Wiesinger, L. I Sacolick, A. Menini, S. S. Kaushik, S. Ahn, P. Veit-Haibach, G. Delso, and D. D. Shanbhag. Zero te mr bone imaging in the head. *Magnetic resonance in medicine*, 75(1):107–114, 2016.

- [11] E. D. Louis. Essential tremor. *The Lancet Neurology*, 4(2):100–110, 2005.
- [12] L. V. Kalia and A. E. Lang. Parkinson’s disease. *The Lancet*, 386(9996):896–912, 2015.
- [13] T. Welton, F. Cardoso, J. A. Carr, L.-L. Chan, G. Deuschl, J. Jankovic, and E.-K. Tan. Essential tremor. *Nature reviews Disease primers*, 7(1):83, 2021.
- [14] B. R. Bloem, M. S. Okun, and C. Klein. Parkinson’s disease. *The Lancet*, 397(10291):2284–2303, 2021.
- [15] D. J. Segar, A. M. Lak, S. Lee, M. Harary, V. Chavakula, P. Lauro, N. McDannold, J. White, and G. R. Cosgrove. Lesion location and lesion creation affect outcomes after focused ultrasound thalamotomy. *Brain*, 144(10):3089–3100, 2021.
- [16] L. Dahmani, Y. Bai, M. Li, J. Ren, L. Shen, J. Ma, H. Li, W. Wei, P. Li, D. Wang, et al. Focused ultrasound thalamotomy for tremor treatment impacts the cerebello-thalamo-cortical network. *npj Parkinson’s Disease*, 9(1):90, 2023.
- [17] Y. Huang, N. Lipsman, M. L. Schwartz, V. Krishna, F. Sammartino, A. M. Lozano, and K. Hynynen. Predicting lesion size by accumulated thermal dose in mr-guided focused ultrasound for essential tremor. *Medical physics*, 45(10):4704–4710, 2018.
- [18] Ltd. InSightec. *Exablate Neuro 4000 Operator’s Manual*. InSightec, Ltd., 5 Nachum Heth St., Tirat Carmel, 39120 Israel, 1st revision edition, April 2021. Available at https://documentation.insightec.com/wp-content/uploads/2020/07/Exablate-4000-Types-1.0-and-1.1-SW7.33-Operator-Manual-CE_0.28.pdf.
- [19] Ltd. InSightec. *Information for Prescribers*. InSightec, Ltd., 5 Nachum Heth St., Tirat Carmel, 39120 Israel, 1st revision edition, September 2022. Available at <https://documentation.insightec.com/wp-content/uploads/E-N-Information-for-Prescribers-PUB41008291-Rev-1.pdf>.
- [20] R. M. Jones, S. Kamps, Y. Huang, N. Scantlebury, N. Lipsman, M. L. Schwartz, and K. Hynynen. Accumulated thermal dose in mri-guided focused ultrasound for essential tremor: repeated sonications with low focal temperatures. *Journal of neurosurgery*, 132(6):1802–1809, 2019.
- [21] E. M Lillie, J. E. Urban, A. A. Weaver, A. K. Powers, and J. D. Stitzel. Estimation of skull table thickness with clinical ct and validation with microct. *Journal of anatomy*, 226(1):73–80, 2015.
- [22] J. E. Urban, A. A. Weaver, E. M. Lillie, J. A. Maldjian, C. T. Whitlow, and J. D. Stitzel. Evaluation of morphological changes in the adult skull with age and sex. *Journal of anatomy*, 229(6):838–846, 2016.

- [23] G. Pinton, J.-F. Aubry, E. Bossy, M. Muller, M. Pernot, and M. Tanter. Attenuation, scattering, and absorption of ultrasound in the skull bone. *Medical physics*, 39(1):299–307, 2012.
- [24] J. Yuen, A. Goyal, T. J. Kaufmann, L. M. Jackson, K. J. Miller, B. T. Klassen, N. Dhawan, K. H. Lee, and V. T. Lehman. Comparison of the impact of skull density ratio with alternative skull metrics on magnetic resonance–guided focused ultrasound thalamotomy for tremor. *Journal of neurosurgery*, 138(1):50–57, 2022.
- [25] P. R. Ng, S. E. Blitz, M. M. J. Chua, and G. R. Cosgrove. Magnetic resonance-guided focused ultrasound thalamotomy for essential tremor patients with low skull density ratio: a case-matched analysis. *Frontiers in Neurology*, 15:1370574, 2024.
- [26] M. D’Souza, K. S. Chen, J. Rosenberg, W. J. Elias, H. M. Eisenberg, R. Gwinn, T. Taira, J. W. Chang, N. Lipsman, V. Krishna, et al. Impact of skull density ratio on efficacy and safety of magnetic resonance–guided focused ultrasound treatment of essential tremor. *Journal of neurosurgery*, 132(5):1392–1397, 2019.
- [27] S. Maesawa, D. Nakatsubo, T. Tsugawa, S. Kato, M. Shibata, S. Takai, J. Torii, T. Ishizaki, T. Wakabayashi, and R. Saito. Techniques, indications, and outcomes in magnetic resonance-guided focused ultrasound thalamotomy for tremor. *Neurologia medico-chirurgica*, 61(11):629–639, 2021.
- [28] N. Vila-Chã, C. Chamadoira, R. Araújo, D. Oliveira, and J. A. Costa. Initial outcomes and safety of mr guided focused ultrasound (mrgfus) thalamotomy for essential tremor of the first fus medical unit in portugal. *Arquivos de Neuro-psiquiatria*, 82(08):001–007, 2024.
- [29] M. Campins-Romeu, R. Conde-Sardón, I. Sastre-Bataller, C. Morata-Martínez, M. Losada-López, J. L. León-Guijarro, L. Raga-Rodríguez, J. Pérez-García, A. Gutiérrez-Martín, A. M. Lozano, et al. Mrgfus subthalamotomy in parkinson’s disease: an approach aimed at minimizing lesion volume. *npj Parkinson’s Disease*, 10(1):1–9, 2024.
- [30] A. Boutet, D. Gwun, R. Gramer, M. Ranjan, G. J. B. Elias, D. Tilden, Y. Huang, S. X. Li, B. Davidson, H. Lu, et al. The relevance of skull density ratio in selecting candidates for transcranial mr-guided focused ultrasound. *Journal of Neurosurgery*, 132(6):1785–1791, 2019.
- [31] N. B. Smith and A. Webb. *Introduction to medical imaging: physics, engineering and clinical applications*. Cambridge university press, 2010.
- [32] T. Shapurian, P. D. Damoulis, G. M. Reiser, T. J. Griffin, and W. M. Rand. Quantitative evaluation of bone density using the hounsfield index. *International Journal of Oral & Maxillofacial Implants*, 21(2), 2006.

- [33] E. C. Herbst, A. A. Felder, L. A. E. Evans, S. Ajami, B. Javaheri, and A. A. Pitsillides. A new straightforward method for semi-automated segmentation of trabecular bone from cortical bone in diverse and challenging morphologies. *Royal Society Open Science*, 8(8):210408, 2021.
- [34] K. Tsai and I. Rachmilevitch. Insightech, private interview, April 2025.
- [35] D. D. Chupova, P. B. Rosnitskiy, O. V. Solontsov, L. R. Gavrilov, V. E. Sinitsyn, E. A. Mershina, O. A. Sapozhnikov, and V. A. Khokhlova. Compensation for aberrations when focusing ultrasound through the skull based on ct and mri data. *Acoustical Physics*, 70(2):288–298, 2024.
- [36] K. Tsai and I. Rachmilevitch. Insightech, private email, March 2025.
- [37] K. Adanty, K. N Rabey, M. R. Doschak, K. B Bhagavathula, J. D. Hogan, D. L. Romanyk, S. Adeeb, S. Ouellet, T. A. Plaisted, S. S. Satapathy, et al. Cortical and trabecular morphometric properties of the human calvarium. *Bone*, 148:115931, 2021.
- [38] F. Wiesinger and M.-L. Ho. Zero-te mri: principles and applications in the head and neck. *The British Journal of Radiology*, 95(1136):20220059, 2022.
- [39] A. Lu, K. R. Gorny, and M.-L. Ho. Zero te mri for craniofacial bone imaging. *American Journal of Neuroradiology*, 40(9):1562–1566, 2019.
- [40] Ü. Aydingöz, A. E. Yıldız, and F. B. Ergen. Zero echo time musculoskeletal mri: technique, optimization, applications, and pitfalls. *Radiographics*, 42(5):1398–1414, 2022.
- [41] M. Weiger and K. P. Pruessmann. Mri with zero echo time. *Emagres*, 2007.
- [42] K. Y. Cheng, D. Moazamian, Y. Ma, H. Jang, S. Jerban, J. Du, and C. B. Chung. Clinical application of ultrashort echo time (ute) and zero echo time (zte) magnetic resonance (mr) imaging in the evaluation of osteoarthritis. *Skeletal radiology*, 52(11):2149–2157, 2023.
- [43] G. Van Rossum and F. L. Drake Jr. *Python tutorial*, volume 620. Centrum voor Wiskunde en Informatica Amsterdam, The Netherlands, 1995.
- [44] Slicer Wiki. Main page/slicercommunity — slicer wiki, 2023. Online; accessed 4-June-2025.
- [45] The SimpleITK Team. A class for registration gui, github. <https://github.com/SimpleITK/TUTORIAL/blob/main/gui.py>, August 2020. Online; accessed 16-April-2025.
- [46] The SimpleITK Team. A class set of methods used for displaying the registration metric during registration the optimization, github. https://github.com/SimpleITK/TUTORIAL/blob/main/registration_gui.py, August 2020. Online; accessed 16-April-2025.

- [47] The SimpleITK Team. Basic registration github. https://github.com/SimpleITK/TUTORIAL/blob/main/05_basic_registration.ipynb, August 2020. Online; accessed 16-April-2025.
- [48] Z. Yaniv, B. C. Lowekamp, H. J. Johnson, and R. Beare. Simpleitk image-analysis notebooks: a collaborative environment for education and reproducible research. *Journal of digital imaging*, 31(3):290–303, 2018.
- [49] P. Thévenaz and M. Unser. Optimization of mutual information for multiresolution image registration. *IEEE transactions on image processing*, 9(12):2083–2099, 2000.
- [50] N. J. Tustison, B. B. Avants, P. A. Cook, Y. Zheng, A. Egan, P. A. Yushkevich, and J. C. Gee. N4itk: improved n3 bias correction. *IEEE transactions on medical imaging*, 29(6):1310–1320, 2010.
- [51] J. Juntu, . Sijbers, D. Van Dyck, and J. Gielen. Bias field correction for mri images. In *Computer Recognition Systems: Proceedings of the 4th International Conference on Computer Recognition Systems CORES'05*, pages 543–551. Springer, 2005.
- [52] S. A. Leung, D. Moore, Y. Gilbo, J. Snell, T. D. Webb, C. H. Meyer, et al. Comparison between mr and ct imaging used to correct for skull-induced phase aberrations during transcranial focused ultrasound. *Nature*, 2022.
- [53] S. Pieper, M. Halle, and R. Kikinis. 3d slicer. In *2004 2nd IEEE international symposium on biomedical imaging: nano to macro (IEEE Cat No. 04EX821)*, pages 632–635. IEEE, 2004.
- [54] S. Weidert, S. Andress, C. Linhart, E. M. Suero, A. Greiner, W. Böcker, C. Kammerlander, and C. A. Becker. 3d printing method for next-day acetabular fracture surgery using a surface filtering pipeline: feasibility and 1-year clinical results. *International Journal of Computer Assisted Radiology and Surgery*, 2020.
- [55] P. Virtanen, R. Gommers, T. E. Oliphant, M. Haberland, T. Reddy, D. Cournapeau, E. Burovski, P. Peterson, W. Weckesser, J. Bright, S. J. van der Walt, M. Brett, J. Wilson, K. Jarrod Millman, N. Mayorov, A. R. J. Nelson, E. Jones, R. Kern, E. Larson, C. J. Carey, I. Polat, Y. Feng, E. W. Moore, J. VanderPlas, D. Laxalde, J. Perktold, R. Cimrman, I. Henriksen, E. A. Quintero, C. R. Harris, A. M. Archibald, A. H. Ribeiro, F. Pedregosa, P. van Mulbregt, and SciPy 1.0 Contributors. SciPy 1.0: Fundamental Algorithms for Scientific Computing in Python. *Nature Methods*, 17:261–272, 2020.
- [56] K. Mitsui, Y. Inoue, H. Itoh, H. Hata, H. Miyatake, and T. Yamane. Relationship between radiation dose indices and patient size in adult brain computed tomography. *Radioprotection*, 60(1):37–43, 2025.

- [57] A. Moreira-Gonzalez, F. E. Papay, and J. E. Zins. Calvarial thickness and its relation to cranial bone harvest. *Plastic and reconstructive surgery*, 117(6):1964–1971, 2006.

A Appendix

Table A1: The structure of the Notebook pipeline, including the 3D Slicer step of the analysis pipeline. The table introduces the Notebook’s name, the data input directory, the output directory as well as the function of the Notebook in question.

| Notebook name | Directories | Function |
|----------------------------------|---|---|
| 01_a_dicom2nifti_MRI.ipynb | CT_data, CT_niftis | Converts CT DICOM to NIFTI and saves to folder. |
| 01_b_dicom2nifti_CT.ipynb | MRI_data, MRI_niftis | Converts MRI and ZTE DICOM to NIFTI and saves separately. |
| 02_trust_but_verify.ipynb | MRI_niftis, CT_niftis | Data quality verification. |
| 03_Coregistration_pipeline.ipynb | registered_output | CT and ZTE registration to MRI space. |
| 04_SDR_calculation.ipynb | registered_output, SDR_data | SDR calculation. |
| 3D Slicer | registered_output | Skull bone mask creation. |
| 05_skull_thickness.ipynb | registered_output, CT_skull_thickness.csv | Skull thickness from CT images. |
| 06_Correlation_analysis.ipynb | SDR_data.csv | Calculate correlation metrics based on SDRs. |

B Appendix

```

interpolator1 = sitk.sitkLinear
interpolator2 = sitk.sitkNearestNeighbor

def register_images(fixed_image, moving_image,
                   interpolator,
                   optimizer_params=None,
                   metric_params=None,
                   shrink_factors=[4,2,1],
                   smoothing_sigmas=[2,1,0]):

    # Initialize transform
    initial_transform = sitk.
        CenteredTransformInitializer(
            fixed_image, moving_image, sitk.AffineTransform
            (3),
            sitk.CenteredTransformInitializerFilter.GEOMETRY
        )

    registration_method = sitk.ImageRegistrationMethod()

    # Metric
    metric_bins = 50 if metric_params is None else
        metric_params.get("bins", 50)
    sampling_pct = 0.01 if metric_params is None else
        metric_params.get("sampling_pct", 0.01)
    registration_method.
        SetMetricAsMattesMutualInformation(
            numberOfHistogramBins=metric_bins)
    registration_method.SetMetricSamplingStrategy(
        registration_method.RANDOM)
    registration_method.SetMetricSamplingPercentage(
        sampling_pct)

    registration_method.SetInterpolator(interpolator1) #
        sitk.sitkLinear

    # Optimizer
    if optimizer_params is None:
        optimizer_params = {"learningRate": 1.0, "
            numberOfIterations": 1000,

```

```

        "convergenceMinimumValue": 1
        e-6, "
        convergenceWindowSize":
        10}
registration_method.SetOptimizerAsGradientDescent(**
    optimizer_params)
registration_method.
    SetOptimizerScalesFromPhysicalShift()

# Multi-resolution
registration_method.SetShrinkFactorsPerLevel(
    shrinkFactors=shrink_factors)
registration_method.SetSmoothingSigmasPerLevel(
    smoothingSigmas=smoothing_sigmas)
registration_method.
    SmoothingSigmasAreSpecifiedInPhysicalUnitsOn()

registration_method.SetInitialTransform(
    initial_transform, inplace=False)

# Connect all for iteration convergence plotting
registration_method.AddCommand(sitk.sitkStartEvent,
    rgui.start_plot)
registration_method.AddCommand(sitk.sitkEndEvent,
    rgui.end_plot)
registration_method.AddCommand(
    sitk.sitkMultiResolutionIterationEvent, rgui.
        update_multires_iterations)
registration_method.AddCommand(
    sitk.sitkIterationEvent, lambda: rgui.
        plot_values(registration_method))

#Obtain transformation
final_transform = registration_method.Execute(
    fixed_image, moving_image)

return final_transform, registration_method

final_tfm_ct, registration_method_ct = register_images(
    mri_image_upsampled, ct_image_norm, interpolator1)
final_tfm_zte, registration_method_zte = register_images
    (mri_image_upsampled, zte_image_norm, interpolator1)

```